Nonlinearly coupled vibrational modes and self-trapped states: Quantum Langevin theory and the single-vibron-oscillator case

Albert M. Clogston
Center for Materials Science, MS K765, Los Alamos National Laboratory, Los Alamos, New Mexico 87545

H. Keith McDowell
CLS-2 MS G738, Los Alamos National Laboratory, Los Alamos, New Mexico 87545
(Received 10 December 1990; revised manuscript received 22 April 1991)

Very great difficulties face a full quantum-theoretical understanding of the problem posed by two nonlinearly interacting vibrational systems at finite temperature. Partial solutions have been obtained in some cases by oversimplification of the defining Hamiltonian or by limiting the Hilbert space of the solution. In this paper we develop an approach to molecular-time-scale generalized-Langevin-equation theory which avoids these approximations. The theory is then applied to the problem of a single-vibron oscillator nonlinearly coupled to a linear chain of coupled molecules. The time correlation function $\dot{\chi}(t)=\mathrm{Re}\langle[c(t),c^{\dagger}(0)]\rangle$ is obtained and its valid time domain determined by comparison with an exact solution of the problem. The valid time domain is shown to be long enough to determine accurate values for the red shift and exponential decay of $\dot{\chi}(t)$ for a wide range of values of parameters including temperature and strength of the nonlinear interaction. An unexpected result is that the exact solution exhibits a slow power-law decay at very low temperatures.

I. INTRODUCTION

An important question in the physics of long chain molecules and pseudo-one-dimensional solids is whether self-consistent symmetry breaking can lead to the formation of localized states, and whether such states are stable against quantum and thermal fluctuations, or at least have a reasonable lifetime that is experimentally significant. The possibility of such localized states was brought into prominence by Davydov in several papers[1-3] where he proposed that such states might exist on one-dimensional molecular chains such as the α-helix because of the nonlinear interaction of the intramolecular carbon-oxygen amide-I stretching modes with low frequency acoustic phonons. We will note later that low-lying optical phonons encountered in molecular crystals such as *l*-alanine can also lead to localized states through nonlinear interactions with acoustic phonons. In the following discussion therefore we will more generally refer to these amide-I stretching modes and low-lying optical phonons as vibron modes.

Davydov proceeded from a simplified Hamiltonian, $H=H(\text{phonon})+H(\text{amide-I})+H(\text{interaction})$, now generally known as the Davydov Hamiltonian, although a similar Hamiltonian was introduced earlier by Fröhlich.[4] In one approach Davydov solved this Hamiltonian system approximately by introducing a product wave function generally known as the Davydov ansatz between a sum of vibron states and a coherent state for the phonons and examining equations of motion derived from the expectation value of the Hamiltonian taken with this wave function. Within appropriate ranges of the parameters defining the acoustic and optical excitations and the nonlinear interaction, Davydov found self-trapping of the carbon-oxygen stretching mode energy by distortion of the lattice. These self-trapped states are generally referred to as solitons though they may not have all the properties of solitary waves.

The assumptions implicit in the Davydov Hamiltonian, Davydov ansatz, the use of the Hamiltonian expectation value, and the conclusions drawn from them have subsequently been challenged from several directions. The first of these has been the introduction of an improved Hamiltonian by Takeno[5] that more accurately describes the physics of the vibron excitations and their interaction with the phonons. In particular, it removes a restriction implicit in the Davydov Hamiltonian that the number of quanta contained in the vibron excitations is conserved. Several papers have been written by Takeno[5] and by Wang, Brown, and Lindenberg[6] that make various approximations, some more serious than others, to examine localized state formation under the dynamics imposed by the Takeno Hamiltonian. The general conclusion of these papers is that solitons governed by the Takeno Hamiltonian are more stable than those governed by the Davydov Hamiltonian.

Davydov's results have also been challenged because of his use of the product wave function mentioned above. An extensive critique of this assumption has been given in a series of papers by Brown, Lindenberg, and West[7,8] who show that the product wave function cannot be a solution of the Schrödinger equation, and that the Davydov ansatz disagrees with exact results that can be obtained in the immobile-exciton limit of the Davydov Hamiltonian. Mechtly and Shaw[9] avoid objections to the Davydov ansatz by a method of solution based on a time-dependent unitary transformation of the Schrödinger equation. Their solution is of limited appli-

cability because it is based on the Davydov Hamiltonian and is restricted to one-phonon states. Another approach by Wagner and Kongeter[10] is also limited by its use of the Davydov Hamiltonian. A paper by Rhodes and Nicholls[11] uses coordinate displacement operators to avoid the Davydov ansatz and claims to show unequivocally that solitons do not move coherently in the α-helix because vibron dispersion dominates the motion. This result is based on an optical phonon Davydov Hamiltonian in which there is no dispersion in phonon modes, and it is not clear the method used can be extended either to the full Davydov Hamitonian with dispersion or to the Takeno Hamiltonian. Moreover it appears to be concerned with the dynamical motion of a single vibron excitation and not the dynamics and lifetime of an extended soliton.

Another problem with the Davydov-Kislukla treatment of solitons on the α-helix is its limitation to one-quantum vibron states.[1-3] An attempt at removing this limitation has been made by Kerr and Lomdahl based on a suggestion by Clogston.[12] This may be an important forward step in the theory because of the possibility that multiquanta solitons are considerably more stable than one-quantum solitons.[12,13] This work has not yet been extended to the Takeno Hamiltonian.

Most of the work referenced above has been concerned with systems at zero degree Kelvin and has not focused on the problem of local state formation and decay at elevated temperatures. Davydov made a calculation of the effects of temperature using a thermally averaged Hamiltonian with results that suggest localized states should continue to exist at temperatures near 300 K.[14] Lomdahl and Kerr have used a finite-temperature molecular dynamics approach to study high-temperature soliton dynamics using the Davydov Hamiltonian.[15] Their general conclusion is that solitons formed in the α-helix system have a very short lifetime of the order of a few picoseconds at 300 K. This result is limited to the parameters appropriate to the α-helix and is not necessarily representative of localized state stability in other coupled vibrational systems, particularly for reasons mentioned in Table I. The calculation also makes use of the Davydov ansatz and may not be representative for that reason. Kerr and Lomdahl have also carried out numerical simulations using the Takeno Hamiltonian and found, consistent with earlier theoretical work, that solitons in this case are more stable than Davydov solitons.[16] In addition Kerr and Lomdahl[12] have performed a molecular dynamics calculation of Davydov solitons for multiple quanta in the vibron system. With their parameters the soliton lifetime is extended from about 3 ps for 2 quanta to 15 ps for 6 quanta, which may be experimentally significant in some cases. These results, however, are again limited by use of the Davydov Hamiltonian and the Davydov ansatz. Alexander and Krumhansl[17] have used a variational approach at finite temperature for computing the states of the Davydov Hamiltonian and find a solitonic solution which produces a spectral intensity whose temperature behavior matches well with the experimental results of Careri *et al.*[18] on acetanilide. Their procedure however does not provide for calculation of the lifetime of the soliton state which must be introduced as an arbitrary assumption into their spectral function. Therefore, one cannot determine whether their solitonic state is short-lived or not. Cruzeiro, Halding *et al.* have also studied the effect of temperature on the Davydov localized states using methods similar to Davydov[19] but with no approximations made beyond that of the Davydov ansatz. They conclude similarly to Davydov[14] that localized states should be stable at 300 K. Another calculation has been made of the lifetime of a Davydov soliton at finite temperature by Cottingham and Schweitzer using a method of partial diagonalization of the Hamiltonian without recourse to the Davydov ansatz.[20] This approach is once again limited by its use of the Davydov Hamiltonian. Their results generally agree with the finding of Kerr and Lomdahl that room temperature α-helix solitons dissipate in picoseconds but seem again to be concerned with a single vibron excitation and not an extended soliton.

TABLE I. Parameter values.

	α-helix (Ref. 14)	l-alanine (Ref. 22)
K (dynes/cm)	13×10^{3}	17×10^{3}
M (amu)[a]	115	89.1
$\hbar\omega_0$ (cm^{-1})	1650	49
$\hbar\omega_a$ (cm^{-1})	88	114
J (cm^{-1})	7.9	5.7
χ (dynes)	0.62×10^{-5}	10^{-7} to 10^{-6}[c]
$\bar{\chi}$ (cm^{-1})[b]	12.7	0.2 to 2.0

[a] 1 amu $=1.6605\times10^{-24}$ g.

[b] See Eq. (12) of text.

[c] This value is uncertain. In principle it can be calculated from the geometric parameters of the l-alanine molecule but this has not yet been done. The value quoted in the table is based on an estimate in Ref. 22 of the minimum possible width of a stable localized state. In this reference it is also shown that $J\sim(l_1-l_0)\chi$ where (l_1-l_0) measures the compression or extension of the hydrogen bond between adjacent molecules in the chain from its neutral length. This is expected to be a small fraction of a lattice constant and is therefore consistent with the values given in the table for l-alanine. It also shows that in some molecular crystals J could be very small while χ remains significantly large. In the table ω_a [see Eq. (10)] is the maximum frequency of the phonon spectrum. A significant difference between the case of l-alanine and α-helix is that in the former case $\omega_0<\omega_a$ while in the latter $\omega_0>\omega_a$.

In view of all these uncertainties one purpose of this paper is to introduce a simple model that can be solved by quantum Langevin theory for all temperatures without recourse to the Davydov ansatz and for either the Davydov or full Takeno Hamiltonian. As described below this model involves a single vibron coupled nonlinearly to a one-dimensional chain of nearest-neighbor coupled molecules. The emphasis will be on the coupling of the vibron to the phonon manifold and in particular on the red-shift of the vibron frequency and the linewidth (or lifetime) of the vibron peak.

It is well known that the interactions of the carbon-oxygen stretching mode (amide-I vibration) with phonons

along one chain of the α-helix leads to the Takeno Hamiltonian[5] which can be written in the form

$$H = H(\text{phonon}) + H(\text{vibron}) + H(\text{interaction}) , \tag{1}$$

where

$$H(\text{phonon}) = \sum_n \left[\frac{1}{2M} p_n^2 + \frac{K}{2}(q_{n+1} - q_n)^2 \right] , \tag{2}$$

$$H(\text{vibron}) = \sum_n [\hbar\omega_0 (c_n^\dagger c_n + \tfrac{1}{2}) + J(c_n^\dagger - c_n)(c_{n+1}^\dagger - c_{n+1})] , \tag{3}$$

and

$$H(\text{interaction}) = -\frac{\chi}{2} \sum_n (c_n^\dagger - c_n)^2 (q_{n+1} - q_{n-1}) . \tag{4}$$

Here p_n and q_n are the momentum and displacement operators of the nth molecule, M is the mass of the chain molecules, and K is the spring constant of the force between molecules. The operators $c_n^\dagger$ and c_n are creation and destruction operators for excitations on the nth oscillator and J is the coupling constant between oscillators. The factor χ is the nonlinear coupling constant between phonons and vibrons and has the dimensions of a force. If the coupling terms in Eqs. (3) and (4) are truncated so that

$$(c_n^\dagger - c_n)(c_{n+1}^\dagger - c_{n+1}) \rightarrow -(c_n^\dagger c_{n+1} + c_n c_{n+1}^\dagger)$$

and

$$(c_n^\dagger - c_n)^2 \rightarrow -(c_n^\dagger c_n + c_n c_n^\dagger) ,$$

then the Takeno Hamiltonian in Eq. (1) reduces to the Davydov Hamiltonian.[1-3]

It is probably less well known, but the nonlinear interaction between acoustic phonons and low-lying optical vibrons acting along the chains in pseudo-one-dimensional molecular crystals such as l-alanine leads to the same Takeno Hamiltonian that applies to the α-helix but with significantly different parameters.[21] To illustrate these differences and to provide a range of parameter values to be used later in Secs. IV and V, a set of values representative of the α-helix and of l-alanine is given in Table I.

The Hamiltonian describing a single vibron oscillator nonlinearly coupled to a phonon manifold is obtained when the Hamiltonian of Eq. (1) is specialized to a single oscillator located at site $n = 0$. The coupling constant J is then equal to zero so that the Hamiltonian of the problem becomes

$$H = \sum_n \left[\frac{1}{2M} p_n^2 + \frac{K}{2}(q_{n+1} - q_n)^2 \right] + \hbar\omega_0 (c^\dagger c + \tfrac{1}{2}) - \frac{\chi}{2}(c^\dagger - c)^2 (q_1 - q_{-1}) , \tag{5}$$

where a subscript has been dropped on the vibron operators and the index n runs from $-N$ to N with N large. If we now introduce second-quantized variables for the phonons by the usual transformations[22]

$$p_n = \sum_{k=-N}^{N} \frac{\exp[2\pi i k n/(2N+1)]}{\sqrt{2N+1}} \times \left[\frac{\hbar M \omega_k}{2} \right]^{1/2} (a_k + a_{-k}^\dagger) \tag{6}$$

and

$$q_n = i \sum_{k=-N}^{N} \frac{\exp[(2\pi i k n/(2N+1)]}{\sqrt{2N+1}} \times \left[\frac{\hbar}{2M\omega_k} \right]^{1/2} (a_k - a_{-k}^\dagger) , \tag{7}$$

we obtain

$$H = \sum_k \hbar\omega_k (a_k^\dagger a_k + \tfrac{1}{2}) + \hbar\omega_0 (c^\dagger c + \tfrac{1}{2}) + (c^\dagger - c)^2 \sum_k \hbar\sigma_k (a_k + a_k^\dagger) , \tag{8}$$

where

$$\omega_k = \left[\frac{2K}{M} \left[1 - \cos\frac{2\pi k}{2N+1} \right] \right]^{1/2} = \omega_a \left| \sin\frac{\pi k}{2N+1} \right| , \tag{9}$$

with

$$\omega_a = 2 \left[\frac{K}{M} \right]^{1/2} \tag{10}$$

and

$$\sigma_k = \frac{2\bar{\chi}}{\hbar} \cos\frac{\pi k}{2N+1} \left[\frac{\sin\frac{\pi k}{2N+1}}{2N+1} \right]^{1/2} \text{sgn } k \tag{11}$$

with

$$\bar{\chi} = \chi \left[\frac{\hbar}{2M\omega_a} \right]^{1/2} . \tag{12}$$

N is the (large) number of molecules in the chain. We note that σ_k has the dimensions of a frequency. If the interaction term in Eq. (8) is truncated so as to drop terms in cc and $c^\dagger c^\dagger$, the Hamiltonian becomes

$$H = \sum_k \hbar\omega_k (a_k^\dagger a_k + \tfrac{1}{2}) + \hbar\omega_0 (c^\dagger c + \tfrac{1}{2}) - (c^\dagger c + c c^\dagger) \sum_k \hbar\sigma_k (a_k + a_k^\dagger) \tag{13}$$

which is a form of the Davydov Hamiltonian adapted to a single-vibron oscillator. This Hamiltonian is identical in form to the Hamiltonian assumed by Brown, Lindenberg, and West to discuss the dynamics of polaron formation in the immobile-exciton limit.[23,24] The Hamiltonian of Eq. (13) is exactly soluble[10,23-25] as will be discussed below and in Sec. III.

It was mentioned above that one purpose of this paper was to bring quantum Langevin theory[26] to bear on the problem of a single-vibron oscillator nonlinearly coupled to a one-dimensional phonon manifold. To this end we have found it necessary to develop a new approach to a

molecular time scale generalized Langevin equation (MTGLE) theory[27–40] which has proved to be particularly powerful and convenient for this class of problem. The second purpose of this paper is to present the details of this new approach which will be done in Sec. II. The method will be applied first in this paper to the Davydov Hamiltonian given by Eq. (13) since this problem can be solved exactly and can be used to test the results of the Langevin theory. In order to make this comparison we have found it necessary to extend earlier work[23,24] on the single oscillator Davydov Hamiltonian, and these results will be summarized in Sec. III. Presentation of results for the red-shift of the vibron oscillator and its lifetime will be given in Sec. IV. These computed quantities will be shown as a function of the ratio of the frequency ω_0 of the vibron oscillator to the maximum frequency ω_a of the phonon band, of the nonlinear coupling constant χ, and of temperature T. In Sec. V these results will be compared with results of the exact theory. The final section will summarize results and draw some conclusions

It is our intention to extend the present work with three additional papers. The first will apply quantum Langevin theory to the single-vibron oscillator coupled to a phonon manifold by the full Takeno interaction term. In this case there is no known exact theory with which to compare, but there should be significant changes in relaxation times due to inclusion of the quantum nonconserving terms $c^\dagger c^\dagger$ and cc. For the second paper we plan to examine the single oscillator Davydov and Takeno cases for the parameter regime of α-helix systems; that is, $\omega_0 \gg \omega_a$. We expect qualitatively different behavior for this case. In the third paper the theory will be extended to the full Hamiltonian including N-coupled vibron oscillators in order to calculate the red-shift and lifetime of a self-trapped soliton state.

II. GENERALIZED LANGEVIN EQUATION THEORY

MTGLE theory[27–40] is founded on the notion that time correlation functions or their spectral density can be built up from short-time or, as originally described by Adelman,[28] from molecular time-scale information. To clarify this notion we recall from previous work that the dipole spectral line shape of a harmonic oscillator coupled to a bath of oscillators is given by[26]

$$S(\omega)=\hbar \exp(\hbar\beta\omega)n(\omega)\rho(\omega)/2m\omega \ , \tag{14}$$

where

$$n(\omega)=[\exp(\hbar\beta\omega)-1]^{-1} \ , \tag{15}$$

$$\rho(\omega)=\frac{2}{\pi}\int_0^\infty dt\,\dot{\chi}(t)\cos\omega t \ , \tag{16}$$

and

$$\dot{\chi}(t)=\tfrac{1}{2}\langle [c(t),c^\dagger(0)]+[c(0),c^\dagger(t)]\rangle \tag{17}$$

with the annihilation (creation) operator $c(t)$ $[c^\dagger(t)]$ defined through Eq. (13). The parameter β is given by $(kT)^{-1}$ where k is the Boltzmann constant and T is the temperature. The brackets $\langle \cdots \rangle$ represent a quantum-statistical canonical-ensemble average. As pointed out,[26] the interpretation of Eq. (14) as being the dipole spectrum depends on one having the relationship $p=m\dot{x}$.[41] The Takeno Hamiltonian in Eq. (8) satisfies this relationship. From Eq. (17), $\dot{\chi}(0)=1$ and we require that $\chi(0)=0$ without loss of generality. We also assume that

$$\lim_{t\to\infty}\dot{\chi}(t)=0 \ .$$

Physically speaking we interpret the correlation function in Eq. (17) and its spectral density in Eq. (16) in terms of an excitation by the operator $c^\dagger$ on a canonical ensemble of systems. For a simple oscillator the response function reduces to $\cos\omega t$, where ω is the frequency of the oscillator, and the excitation has an infinite lifetime. For more general condensed matter systems we generally expect the response function to behave as a damped oscillation with the form $e^{-t/\tau}\cos\omega t$ where τ is a temperature dependent lifetime. Clearly, we can make other choices for the excitation operator in Eq. (17) and use MTGLE theory to study the lifetimes and spectral line shapes of rather general excitations of condensed matter systems. This strategy will be employed in subsequent papers to examine the stability of localized vibrations or solitons. For the present we consider only the simple excitation $c^\dagger$ in order to build up an understanding of the nonlinear effects from the Hamiltonian in Eq. (13).

A. General considerations

The computation of time correlation response functions or their spectral densities by the MTGLE approach is accomplished through the processing of short-time derivatives of the function $\dot{\chi}(t)$ defined in Eq. (17).[37] These derivatives (or moments) are given by[37]

$$\sigma_0^{(n)}=(-1)^n\dot{\chi}^{(2n)}(0) \tag{18}$$

$$=\langle [c^{(n)}(0),c^{(n)\dagger}(0)]\rangle \ , \tag{19}$$

where

$$\dot{\chi}^{(2n)}(0)=\left[\left[\frac{d}{dt}\right]^{2n}\dot{\chi}(t)\right]_{t=0} \tag{20}$$

and

$$c^{(n)}(0)=\left.\frac{d^n c(t)}{dt^n}\right|_{t=0} \ . \tag{21}$$

If we invert Eq. (16) we have

$$\dot{\chi}(t)=\int_0^\infty d\omega\,\rho(\omega)\cos\omega t \tag{22}$$

so that also

$$\sigma_0^{(n)}=\int_0^\infty d\omega\,\omega^{2n}\rho(\omega) \ . \tag{23}$$

From Eq. (16) we have by partial integration

$$\rho(\omega)=\frac{2\omega}{\pi}\int_0^\infty dt\,\chi(t)\sin\omega t \ . \tag{24}$$

If the Laplace transform of $\chi(t)$ is indicated by $\hat{\chi}(z)$, we then have

$$\rho(\omega)=-\frac{2\omega}{\pi}\mathrm{Im}\hat{\chi}(i\omega)\ . \tag{25}$$

The problem of finding the spectral line shape is thus reduced to finding the Laplace transform of $\chi(t)$. To this end we define a hierarchy of heat-bath functions $\theta_m(t)$ by the equations[37] [the constants $\omega_{e_m}^2$ and $\omega_{c_{m+1}}^4$ are defined in Eq. (41)]

$$\hat{\chi}(z)=[z^2+\omega_{e_0}^2-\omega_{c_1}^4\hat{\theta}_1(z)]^{-1}\ , \tag{26}$$

$$\hat{\theta}_m(z)=[z^2+\omega_{e_m}^2-\omega_{c_{m+1}}^4\hat{\theta}_{m+1}(z)]^{-1}\ . \tag{27}$$

In analogy with Eqs. (16), (18), (22), (23), (24), and (25) we have

$$\rho_m(\omega)=\frac{2}{\pi}\int_0^\infty dt\ \dot{\theta}_m(t)\cos\omega t\ , \tag{28}$$

$$\sigma_m^{(n)}=(-1)^n\dot{\theta}_m^{(2n)}(0)\ , \tag{29}$$

$$\dot{\theta}_m(t)=\int_0^\infty d\omega\,\rho_m(\omega)\cos\omega t\ , \tag{30}$$

$$\sigma_m^{(n)}=\int_0^\infty d\omega\,\omega^{2n}\rho_m(\omega)\ , \tag{31}$$

$$\rho_m(\omega)=\frac{2\omega}{\pi}\int_0^\infty dt\ \theta_m(t)\sin\omega t\ , \tag{32}$$

and

$$\rho_m(\omega)=-\frac{2\omega}{\pi}\mathrm{Im}\hat{\theta}_m(i\omega)\ . \tag{33}$$

From Eq. (26) we have immediately

$$\hat{\chi}(i\omega)=\frac{1}{\omega_{e_0}^2-\omega^2-\omega_{c_1}^4\hat{\theta}_1(i\omega)}\ . \tag{34}$$

If we define

$$I(\omega)=\omega_{c_1}^4\mathrm{Im}\hat{\theta}_1(i\omega) \tag{35a}$$

and

$$R(\omega)=\omega_{c_1}^4\mathrm{Re}\hat{\theta}_1(i\omega)\ , \tag{35b}$$

then

$$\rho(\omega)=-\frac{2\omega}{\pi}\frac{I(\omega)}{[\omega_{e_0}^2-\omega^2-R(\omega)]^2+[I(\omega)]^2}\ . \tag{36}$$

To determine the position of the peak $\omega_{\max}$ in Eq. (36) we use the relation

$$\omega_{e_0}^2-\omega_{\max}^2-R(\omega_{\max})=0\ . \tag{37}$$

If we assume that $R(\omega)=R(\omega_{\max})$ and $I(\omega_{\max})$ over the region of the resonance, then

$$\rho(\omega)\sim\frac{1}{\pi}\frac{\left[-\dfrac{I(\omega_{\max})}{2\omega_{\max}}\right]}{[\omega-\omega_{\max}]^2+\left[\dfrac{I(\omega_{\max})}{2\omega_{\max}}\right]^2} \tag{38}$$

for $\omega>0$ and one identifies the lifetime as

$$\frac{1}{\tau}=-\frac{I(\omega_{\max})}{2\omega_{\max}}\ . \tag{39}$$

B. Calculation of $\dot{\theta}_1(t)$ and $\rho_1(\omega)$

Using the Laplace transforms defined in Eqs. (26) and (27), the moments defined in Eq. (29) can be calculated recursively from the relation[27]

$$\sigma_{m-1}^{(n)}=\omega_{e_{m-1}}^2\sigma_{m-1}^{(n-1)}+\omega_{c_m}^4\sum_{j=0}^{n-2}\sigma_m^{(j)}\sigma_{m-1}^{(n-2-j)} \tag{40}$$

where

$$\omega_{e_m}^2=\sigma_m^{(1)}\ , \tag{41a}$$

and

$$\omega_{c_{m+1}}^4=\sigma_m^{(2)}-(\sigma_m^{(1)})^2\ . \tag{41b}$$

A new set of functions $Q_m(t)$ is defined by the relations

$$Q_1(t)=\theta_1(t)\ , \tag{42a}$$

and

$$Q_m(t)=\omega_{c_m}^2\int_0^t d\tau\,\theta_m(t-\tau)Q_{m-1}(\tau)\ ,\quad m>1\ , \tag{42b}$$

from which it can be shown that[37]

$$\ddot{\underline{Q}}(t)=-\underline{M}\underline{Q}(t)\ , \tag{43}$$

where

$$\underline{Q}(t)=\begin{bmatrix}Q_1(t)\\Q_2(t)\\Q_3(t)\\\cdot\end{bmatrix} \tag{44}$$

and $\underline{M}$ is the symmetric tridiagonal matrix

$$\underline{M}=\begin{bmatrix}\omega_{e_1}^2 & -\omega_{c_2}^2 & 0 & 0\\ -\omega_{c_2}^2 & \omega_{e_2}^2 & -\omega_{c_3}^2 & 0\\ 0 & -\omega_{c_3}^2 & \omega_{e_3}^2 & \cdots\\ 0 & 0 & \cdots & \cdots\end{bmatrix}\ . \tag{45}$$

Suppose that a transformation $\underline{T}$ is introduced that diagonalizes $\underline{M}$ so that

$$\underline{T}\underline{M}\underline{T}^T=\underline{M}_D\ , \tag{46}$$

where $\underline{M}_D$ has the diagonal eigenvalues $\omega_1^2, \omega_2^2, \omega_3^2, \ldots$. It can be shown[37] that

$$\dot{\theta}_1(t)=\sum_n(T_{n1})^2\cos\omega_n t \tag{47}$$

and

$$\rho_1(\omega)=\sum_n(T_{n1})^2\delta(\omega-\omega_n)\ . \tag{48}$$

In principle the nested heat baths defined by Eqs. (27) can be continued indefinitely so that the dimension N of the matrix $\underline{M}$ is infinite and the sums in Eqs. (47) and (48) are over an infinite set of eigenvalues ω_n. In practice, computational difficulties in calculating the Einstein and coupling frequencies in Eqs. (41a) and (41b) limit the number of moments $\sigma_1^{(n)}$ that can be used in Eq. (40), and

thereby limit the dimension of the matrix $\underline{M}$ and the number of eigenvalues ω_n that can be calculated. If n moments are used, $N=(n+1)/2$ heat baths can be calculated and the matrix $\underline{M}$ has dimensions $N\times N$ and N eigenvalues. A typical value for the present calculations is $n=13$ which leads to a square matrix of dimension 7, with 7 eigenvalues. As will be seen this limit places a corresponding limit on the time interval over which the MTGLE calculation of the time-correlation function $\dot{\chi}(t)$ remains valid.

C. MTGLE representation of $\dot{\theta}_m(t)$

We now turn to a different representation of $\dot{\theta}_m(t)$. We introduce first a set of functions $G_k(t)$ which will be called generalized Langevin equation (GLE) functions and are defined by the integral equation

$$G_k(t)=\frac{1}{\pi}\int_0^{\pi}dx\,[\cos(k-1)x-\cos(k+1)x]\frac{\sin\Omega t}{\Omega}\ , \tag{49}$$

where

$$\Omega=\sqrt{\omega_e^2-2\omega_c^2\cos x} \tag{50}$$

and ω_e and ω_c are constants to be determined later. The Laplace transform of $G_k(t)$ is easily shown to be

$$\hat{G}_k(z)=\frac{1}{\omega_c^2}\left[\frac{1}{2\omega_c^2}[z^2+\omega_e^2-\sqrt{(z^2+\omega_e^2)^2-4\omega_c^4}\,]\right]^k . \tag{51}$$

In the special case $\omega_e^2=2\omega_c^2$ which will be sometimes encountered below, we have

$$\hat{G}_k(z)=\frac{4}{(2\omega_e^2)^{k+1}}[z-\sqrt{z^2+2\omega_e^2}\,]^{2k} \tag{52}$$

which will be recognized as the Laplace transform of

$$\frac{4k}{\omega_e^2 t}J_{2k}(\sqrt{2}\,\omega_e t)\ .$$

Thus the $G_k(t)$ functions are a generalization of Bessel functions and share some of their properties. As will be shown, it is the time derivatives $\dot{G}_k(t)$ which are used to fit correlation functions. An important aspect of $\dot{G}_k(t)$ is that for large k its onset is delayed until a time given approximately by

$$\omega_e t=k\left[\frac{\omega_e}{\omega_c}\right]^2 . \tag{53}$$

This relationship can be obtained directly from the definition of $G_k(t)$ in Eq. (49).

We next expand the heat-bath functions $\theta_m(t)$ in the generalized Langevin functions as follows:

$$\theta_m(t)=\sum_{k=1}^{\infty}\alpha_k^{(m)}G_k(t) \tag{54}$$

so that

$$\dot{\theta}_m^{(2n)}(0)=\sum_{k=1}^{\infty}\alpha_k^{(m)}\dot{G}_k^{(2n)}(0)\ . \tag{55}$$

The derivatives $\dot{G}_k^{(2n)}(0)$ can be obtained from Eq. (49) and are given by

$$\dot{G}_k^{(2n)}(0)=\frac{k}{2}(-1)^{n+k+1}n!\omega_e^{2n}\sum_{j=0}^{\infty}\left[\frac{\omega_c}{\omega_e}\right]^{2j}\frac{[1-(-1)^{k+j}]}{(n-j)!\left[\frac{j+k+1}{2}\right]!\left[\frac{j-k+1}{2}\right]!}\ . \tag{56}$$

It is easy to see that $\dot{G}_k^{(2n)}(0)=0$ for $k>n+1$. Thus, combining Eqs. (29), (55), and (56), the coefficients $\alpha_k^{(m)}$ can be obtained recursively from the moments $\sigma_m^{(n)}$ in such a way that $n+1$ coefficients are obtained from n moments. It can then be shown that the Laplace transforms

$$\hat{\theta}_m(z)=\sum_{k=1}^{\infty}\alpha_k^{(m)}G_k(z) \tag{57}$$

satisfy the heat-bath hierarchy Eqs. (27). Thus, if the series in Eq. (54) for $m=1$ converges, its derivative is a representation of $\dot{\theta}_1(t)$. Because computational difficulties limit the number of $\alpha_k^{(1)}$ coefficients that can be accurately calculated, it is important that the series representation of $\dot{\theta}_1(t)$ be as rapidly convergent as possible. In the next section we will show how this can be achieved by adjusting the parameters ω_e and ω_c.

Once ω_e and ω_c have been fixed we can carry out a sequence of computations in which successively larger numbers of terms are included in the series expansion of $\dot{\theta}_1(t)$, or alternatively the Laplace transform $\hat{\theta}_1(z)$, which can then be used in Eqs. (35a) and (35b) to calculate $I(\omega)$ and $R(\omega)$ and thereby $\omega_{\max}$ and τ from Eqs. (36), (37), and (39). The end results are rapidly convergent series with increasing k for $\omega_{\max}$ and τ which demonstrate that an accurate representation of $\dot{\theta}_1(t)$ has been achieved. It also suggests that the series representation of $\dot{\theta}_1(t)$ remains a good approximation for very much larger values of k, and this fact will be demonstrated by comparison with the exact theory in Sec. V.

To achieve the MTGLE representation of $\dot{\theta}_1(t)$ described in this section, it is necessary that one compute the moments $\sigma_1^{(n)}$. As shown in Sec. II B, these moments are computed recursively using Eq. (40) from the short-time derivatives $\sigma_0^{(n)}$ of the time-correlation function $\dot{\chi}(t)$. The explicit computation of the quantities $\sigma_0^{(n)}$ for the Hamiltonian in Eq. (13) is presented in the Appendix.

D. Matching spectral density functions

From Eqs. (51) and (57) we have

$$\hat{\theta}_1(i\omega)=\frac{1}{\omega_c^2}\sum_{k=1}^{\infty}\alpha_k\left[\frac{1}{2\omega_c^2}[\omega_e^2-\omega^2-\sqrt{(\omega_e^2-\omega^2)^2-4\omega_c^4}]\right]^k , \tag{58}$$

where the superscript on α_k has been dropped for convenience. Equation (58) can be put into the form

$$\hat{\theta}_1(i\omega)=\frac{1}{\omega_c^2}\sum_{k=1}^{\infty}\alpha_k(\cosh k\phi-\sinh k\phi);\quad \omega^2<(\omega_e^2-2\omega_c^2),\quad \cosh\phi=\frac{1}{2\omega_c^2}(\omega_e^2-\omega^2) , \tag{59a}$$

$$\hat{\theta}_1(i\omega)=\frac{1}{\omega_c^2}\sum_{k=1}^{\infty}\alpha_k(\cos k\phi-i\sin k\phi);\quad (\omega_e^2-2\omega_c^2)<\omega^2<(\omega_e^2+2\omega_c^2),\quad \cos\phi=\frac{1}{2\omega_c^2}(\omega_e^2-\omega^2) , \tag{59b}$$

and

$$\hat{\theta}_1(i\omega)=\frac{1}{\omega_c^2}\sum_{k=1}^{\infty}\alpha_k(-1)^k(\cosh k\phi+\sinh k\phi);\quad \omega^2>(\omega_e^2+2\omega_c^2),\quad \cosh\phi=\frac{1}{2\omega_c^2}(\omega^2-\omega_e^2) . \tag{59c}$$

These three equations determine $I(\omega)$ and $R(\omega)$ defined in Eqs. (35a) and (35b). In particular $\rho_1(\omega)$ defined by Eq. (33) is nonzero only for ω^2 in the range $(\omega_e^2-2\omega_c^2)<\omega^2<(\omega_e^2+2\omega_c^2)$ and is given by

$$\rho_1(\omega)=\frac{2\omega}{\pi\omega_c^2}\sum_{k=1}^{\infty}\alpha_k\sin k\phi(\omega) , \tag{60}$$

where

$$\cos\phi(\omega)=\frac{1}{2\omega_c^2}(\omega_e^2-\omega^2) . \tag{61}$$

It is easily confirmed from Eqs. (60) and (61) that

$$\int_0^{\infty}d\omega\,\rho_1(\omega)=1 .$$

For computational reasons discussed above the number of terms in this series will be limited to $k=2N$. We therefore define a spectral density function $\rho_1^*(\omega)$ by the finite series

$$\rho_1^*(\omega)=\frac{2\omega}{\pi\omega_c^2}\sum_{k=1}^{2N}\alpha_k\sin k\phi(\omega) . \tag{62}$$

It is easy to show in the same way that $\rho_1^*(\omega)$ also has the property

$$\int_0^{\infty}d\omega\,\rho_1^*(\omega)=1 .$$

We next define a spectral density function $\tilde{\rho}_1(\omega)$ corresponding to Eq. (48) but taking into account the finite dimension N of the matrix $\underline{M}$:

$$\tilde{\rho}_1(\omega)=\sum_{n=1}^{N}(T_{n1})^2\delta(\omega-\omega_n) . \tag{63}$$

From Eq. (63) $(T_{n1})^2$ can then be obtained in the form

$$(T_{n1})^2=\int_{(\omega_n+\omega_{n-1})/2}^{(\omega_{n+1}+\omega_n)/2}d\omega\,\tilde{\rho}_1(\omega) , \tag{64}$$

where

$$\omega_0=\sqrt{\omega_e^2-2\omega_c^2} \tag{65a}$$

and

$$\omega_{N+1}=\sqrt{\omega_e^2+2\omega_c^2} . \tag{65b}$$

If the matrix $\underline{M}$ is limited to dimensions $N\times N$, it can still be proved that

$$\dot{\theta}_1^{(2n)}(0)=(-1)^n\sum_{m=1}^{N}(T_{n1})^2\omega_m^{2n} . \tag{66}$$

Since $\dot{\theta}_1(0)=1$ this leads to the result

$$\sum_{n=1}^{N}(T_{n1})^2=1 \tag{67}$$

which implies through Eq. (64) that

$$\int_0^{\infty}d\omega\,\tilde{\rho}_1(\omega)=1 .$$

The form of Eq. (64) suggests a procedure for defining the parameters ω_e and ω_c which are used in the generalized Langevin functions, namely, we compute a trial spectral weight depending on the undetermined constants ω_e and ω_c by the integral

$$(T_{n1}^*)^2=\int_{(\omega_n+\omega_{n-1})/2}^{(\omega_{n+1}+\omega_n)/2}d\omega\,\rho_1^*(\omega) . \tag{68}$$

In Eq. (64) we can choose any end points for the integral which lie between the eigenfrequencies. On the other hand the choice of end points in Eq. (68) affects the computed results for the spectral weights $(T_{n1}^*)^2$. We have chosen to use the midpoints in order to achieve a reasonably uniform histograming of the spectral density $\rho_1^*(\omega)$. Substituting Eq. (62) into Eq. (68) yields after simple integration

$$(T_{n1}^*)^2=\frac{2}{\pi}\sum_{k=1}^{2N}\alpha_k\int_{\phi_n}^{\phi_{n+1}}d\phi\sin\phi\sin k\phi=\frac{1}{\pi}\sum_{k=1}^{2N}\alpha_k\left[\frac{\sin(k-1)\phi_{n+1}}{k-1}-\frac{\sin(k+1)\phi_{n+1}}{k+1}-\frac{\sin(k-1)\phi_n}{k-1}+\frac{\sin(k+1)\phi_n}{k+1}\right] , \tag{69}$$

where

$$\phi_n = \arccos\left[\frac{\omega_e^2 - [\frac{1}{2}(\omega_n + \omega_{n-1})]^2}{2\omega_c^2}\right] . \tag{70}$$

We now fix the values of ω_e and ω_c by minimizing the objective function

$$F(\omega_e,\omega_c) = \sum_{n=1}^{N} [(T_{n1})^2 - (T_{n1}^*)^2] . \tag{71}$$

We use the Levenberg-Marquardt method[42] to achieve minimization. We have found that the best fit often produces a spectral density $\rho_1^*(\omega)$ which is highly oscillatory. To damp this down and produce a smooth fit, we constrain the end points in Eqs. (65), which in principle should change as ω_e and ω_c change, to have the values ω_1 and ω_N in Eq. (68). This additional constraint serves to produce both a good fit and eliminate the oscillations. In the final analysis, of course, it does not matter how one obtains ω_e and ω_c as long as the final choice produces smooth convergence of $\omega_{\max}$ and the lifetime τ as one increases the number of generalized Langevin functions used in Eq. (54) for $\theta_1(t)$. We anticipate that fitting methods other than the one used in Eq. (71) will also work well.

To display graphically the fit which we achieve, it is useful to rewrite the exact spectral density $\rho_1(\omega)$ given by Eq. (48) for N indefinitely large in the form

$$\rho_1(\omega) = \int_0^\infty d\omega_n (T_{n1})^2_{\omega_n} \left[\frac{dn}{d\omega_n}\right]_{\omega_n} \delta(\omega - \omega_n) \tag{72}$$

$$= (T_{n1})^2_{\omega} \left[\frac{dn}{d\omega}\right]_{\omega} , \tag{73}$$

where $(dn/d\omega)$ is the density of closely spaced eigenvalues at frequency ω. For the case of a limited number of eigenvalues N this suggests that we define an analogous spectral density $\rho_1'(\omega_n)$ by the relation

$$\rho_1'(\omega_n) = (T_{n1})^2 \frac{2}{\omega_{n+1} - \omega_{n-1}} . \tag{74}$$

We find empirically that when our optimization fitting procedure is used $\rho_1^*(\omega)$ gives a very close fit to $\rho_1'(\omega_n)$ at $\omega = \omega_n$. This is shown in Fig. 1 for a case which is described in detail in Sec. IV. It is easy to see that this is to be expected from Eq. (68) which leads to the following approximate expression for $(T_{n1}^*)^2$:

$$(T_{n1}^*)^2 \cong \rho_1^*(\omega_n) \frac{\omega_{n+1} - \omega_{n-1}}{2} . \tag{75}$$

In part this good fit is because $\rho_1^*(\omega)$ has been constructed to have the same spectral moments as $\tilde{\rho}_1(\omega)$. In addition, however, the spectral density $\tilde{\rho}_1(\omega)$ given by Eq. (63) can be expanded in the Fourier sine series complete in the range $\phi = 0$ to π as

$$\tilde{\rho}_1(\omega) = \frac{2\omega}{\pi\omega_c^2} \sum_{k=1}^{\infty} \bar{\alpha}_k \sin k\phi(\omega) \tag{76}$$

analogous to Eq. (62), except that k runs from 1 to ∞. Then it is easy to prove using Eqs. (61) and (66) that $\bar{\alpha}_k = \alpha_k$ for $k \le 2N$. Thus, whatever the assigned values of ω_e and ω_c, $\rho_1^*(\omega)$ is always equal to the discrete spectral density given by Eq. (62) when it is smoothed by truncating the series in Eq. (76) at $k = N$. The spectral density $\rho_1^*(\omega)$ is therefore not only a smoothed version of $\tilde{\rho}_1(\omega)$ but is also optimally smoothed by optimizing the spectral weight assigned to each frequency interval $\frac{1}{2}(\omega_n + \omega_{n-1})$ to $\frac{1}{2}(\omega_{n+1}\omega_n)$.

It is evident that $\rho_1'(\omega)$ becomes a better approximation to $\rho_1(\omega)$ as N increases. In that case, to the extent that $\rho_1^*(\omega)$ remains a close fit to $\rho_1'(\omega)$, $\rho_1^*(\omega)$ also approaches $\rho_1(\omega)$ as N increases. This is shown convincingly in Fig. 24 where the solid line is a numerical calculation of $\rho_1(\omega)$ from the exact theory. The superimposed dots are values of $\rho_1^*(\omega)$ calculated as described above using parameters given in Sec. IV, Set 1. This remarkably close fit to the exact $\rho_1(\omega)$, particularly around the important region near $\omega/\omega_0 = 1$, has been achieved using 15 moments of $\dot{\chi}(t)$.

III. EXACT SOLUTION OF THE SINGLE VIBRON OSCILLATOR PROBLEM WITH A DAVYDOV HAMILTONIAN

As pointed out by Brown, Lindenberg, and West,[23,24] Hamiltonians of the single-vibron form given in Eq. (13) can be diagonalized by a canonical transformation and are therefore exactly soluble. In order to provide some exact results which can be compared with results obtained from the MTGLE theory developed in Sec. II, we have obtained more explicit results than provided by Brown *et al.*,[23,24] particularly for the time-correlation function $\dot{\chi}(t)$ and for elevated temperature. These results will be published separately and will therefore only be outlined briefly in this section. As seen below, a particularly interesting result is that $\dot{\chi}(t)$ does not decrease exponentially with time at absolute zero but rather falls off as a small power of time.

We have derived elsewhere[43] that

$$\dot{\chi}(t) = \frac{e(t)}{Q} \sum_n e^{-\beta E_n} \left[(n+1)\cos\left[[\omega_0 - 8\eta(n+1)]t + 4\sum_k \frac{\sigma_k^2}{\omega_k^2}\sin\omega_k t\right] - n\cos\left[(\omega_0 - 8\eta n)t - 4\sum_k \frac{\sigma_k^2}{\omega_k^2}\sin\omega_k t\right]\right] , \tag{77}$$

where

$$E_n = \hbar\omega_0(n + \tfrac{1}{2}) - \hbar(2n+1)^2\eta , \tag{78}$$

$$e(t) = \exp\left[4\sum_k \frac{\sigma_k^2}{\omega_k^2}(\cos\omega_k t - 1)\coth\left[\frac{\hbar\beta\omega_k}{2}\right]\right] , \tag{79}$$

$$\eta = \sum_k \frac{\sigma_k^2}{\omega_k} , \tag{80}$$

and

$$Q=\sum_n e^{-\beta E_n} . \tag{81}$$

It should be noted that the partition function sum in Eq. (81) must be truncated at some large value of n since the energy E_n eventually becomes large and negative. This is an artifact of the simple polynomial potential energy expression used in Davydov-type models, but is of no practical effect up to temperatures of order 300 K. The expression in Eq. (77) is an exact analytic form for $\chi(t)$. In the Appendix this form is used for convenience to compute the required MTGLE time derivatives in Eq. (18).

We have also shown elsewhere[43] that the behavior of $\dot{\chi}(t)$ following a short initial transient can be found exactly from Eq. (77). When σ_k is given by Eq. (11) the behavior of the exponential part $e(t)$ for $\omega_a t > 2\pi$ is given by

$$e(t)=\exp\left[-\left[\frac{16\bar{\chi}^2}{\hbar^2\omega_a^2}\right]\left\{0.172\,118+\frac{2}{\pi}\ln\frac{\omega_a\hbar\beta}{2\pi}+\frac{2}{\pi}\ln\left[1-\exp\left[-\frac{2\pi t}{\hbar\beta}\right]\right]+\frac{2t}{\hbar\beta}\right\}\right] . \tag{82}$$

For $2\pi t \gg \hbar\beta$ this becomes

$$e(t)=\exp\left[-\frac{32\bar{\chi}^2}{\omega_a^2\hbar^3\beta}t\right] \tag{83}$$

so that the exponential lifetime can be identified as

$$\tau=\frac{\omega_a^2\hbar^3\beta}{32\bar{\chi}^2} . \tag{84}$$

For $2\pi t \ll \hbar\beta$ but t still sufficiently large to be beyond the initial transient, the decay is no longer exponential and is given approximately by

$$e(t)=(\omega_a t)^{-32\bar{\chi}^2/\pi\hbar^2\omega_a^2}\exp\left[-\frac{2.753\,888\bar{\chi}^2}{\hbar^2\omega_a^2}\right] . \tag{85}$$

Therefore at very low temperatures there is an extended range through which $\dot{\chi}(t)$ decreases as a small power of t.

The long-time behavior of the prefactor in Eq. (77), which contains a statistical average, has also been examined in detail elsewhere.[43] In summary we find that the prefactor, which we denote as $p(t)$, for $\omega_a t > 2\pi$ behaves essentially as

$$p(t)=\frac{2\cos\{\omega_0 t-2\tan^{-1}[(2n(\omega_b)+1)\tan 4\eta t]\}}{1+[2n(\omega_b)+1]^2+\{1-[2n(\omega_b)+1]^2\}\cos 8\eta t} , \tag{86}$$

where

$$\omega_b=\omega_0-4\eta , \tag{87}$$

and $n(\omega_b)$ is given in Eq. (15). For times small enough that $\frac{1}{6}n(\omega_b)(8\eta t)^3 \ll 1$, the frequency of oscillation in the numerator is easily found to be

$$\omega=\omega_0-[2n(\omega_b)+1]8\eta . \tag{88}$$

We anticipate that the frequency in Eq. (88) will predict the location of MTGLE peaks, $\omega_{\max}$, since MTGLE is based on a short-time approach. The correspondence of τ in Eq. (84) and $\omega_{\max}$ in Eq. (88) with values calculated from the MTGLE theory will be discussed in Secs. IV and V.

The preceding discussion of the exact solution for the time-correlation function $\dot{\chi}(t)$ brings out that there are four time scales involved in the problem of a single vibron coupled nonlinearly to a phonon lattice. The first is the period $2\pi/\omega_0$ associated with the uncoupled frequency of the vibron. The second is a characteristic reaction time of the phonon lattice $2\pi/\omega_a$ which governs the short-time transients of $\dot{\chi}(t)$. The third is the time $\hbar\beta/2\pi$ which governs the transition from small power law to exponential decay of $\dot{\chi}(t)$ and which is generally recognized as the time scale of decay of quantum fluctuations. It is interesting that this time scale emerges in the current problem but does not play a part in the decay of $\dot{\chi}(t)$ for the corresponding linearly coupled problem.[26] Finally there is the time scale associated with Eq. (86) which determines when the frequency of oscillation of $\dot{\chi}(t)$ diverges from the frequency given by Eq. (88). This is also the time scale limiting the valid time domain of MTGLE theory.

IV. RESULTS CALCULATED FROM MTGLE THEORY

In this section we will present a selection of results for the single-vibron case (specialized to the Davydov Hamiltonian) calculated from MTGLE theory. In most cases these results include the spectral density function $\rho_I^*(\omega)$, the red-shifted oscillation frequency $\omega_{\max}$, and the relaxation time τ. Since the results depend on four parameters ω_a, ω_0, $\bar{\chi}$, and T, the selection of results has necessarily to be quite sparse, but has been chosen to be representative. The red-shifted oscillation frequency is obtained from the maximum of the spectral-density function $\rho(\omega)$ given by Eq. (36), although this is always equal to the positive root of Eq. (37). The relaxation time τ is calculated from Eq. (39). The results presented below are grouped for convenience into nine different sets each intended to illustrate some features of the MTGLE calculations.

TABLE II. Eigenfrequencies and spectral weights of first heat bath at fourth order. The parameters used are $\hbar\omega_a=60$ cm^{-1}, $\hbar\omega_0=30$ cm^{-1}, $\bar{\chi}=0.3$ cm^{-1}, and $T=50$ K.

n	ω_n/ω_0	$\lvert T_{n1}\rvert^2$
1	0.802 141	0.066 794
2	1.554 953	0.238 288
3	2.215 438	0.389 135
4	2.739 373	0.297 269
5	3.217 986	0.008 337
6	4.222 060	0.000 163
7	4.716 044	0.000 015

Set 1: The set comprises three figures and one table and is intended to show a typical set of results at moderate temperature. The parameters chosen are $\hbar\omega_a = 60\ \mathrm{cm}^{-1}$, $\hbar\omega_0 = 30\ \mathrm{cm}^{-1}$, $\bar{\chi} = 0.3\ \mathrm{cm}^{-1}$, and $T = 50$ K. The results are calculated to fourth order in the coupling constant. Table II lists the N eigenfrequencies and spectral weights obtained by diagonalization of the moment matrix $\underline{M}$ given by Eq. (45). The fit of the spectral density function $\rho_1^*(\omega)$ to the spectral density at the N eigenfrequencies is shown in Fig. 1. This determines the parameters $(\omega_e/\omega_0)^2 = 11.429$ and $(\omega_c/\omega_0)^4 = 32.646$. Figures 2 and 3 show the calculated values of $\omega_{\max}$ and τ as a function of the GLE expansion index k for the fixed values of ω_e and ω_c given above. The important thing to note here is the rapid convergence of these quantities as k increases. The excellent fit in Figs. 2 and 3 of the converged values to values predicted from the exact theory will be shown in more detail in Sec. V.

Set 2: This set of results comprises three figures calculated using the same parameters as set 1, but calculated to only second order in the coupling constant. The graph of $\rho_1^*(\omega)$ as shown in Fig. 4 is nearly identical to the fourth-order result in Fig. 1. The main effect of the fourth-order calculation has been to add some high-frequency oscillations to $\rho_1^*(\omega)$ which are irrelevant to the calculation of $\omega_{\max}$ and τ. Correspondingly the converged values of $\omega_{\max}$ and τ shown in Fig. 5 and 6 are essentially identical whether calculated to second or fourth order.

Set 3: This set of results is given in Table III which shows values of ω_{e_N} and ω_{c_N} calculated for second, fourth, and all orders in the coupling constant using results from the exact theory outlined in Sec. III. The point of the table is to show that the Einstein frequencies and coupling frequencies from Eqs. (41a) and (41b) show very little change in going from fourth order to all orders up to the highest bath index that can be calculated to all orders. We therefore conclude based on agreement of results in sets 1 and 2 and the small changes in ω_{e_N} and ω_{c_N} going from fourth to all orders that one need only compute results through fourth order to get numerical convergence for the current parameter regime.

Set 4: This set of results is included to show how $\rho_1^*(\omega)$, $\omega_{\max}$, and τ vary for different values of the vibron oscillator frequency ω_0. The values of the parameters adopted

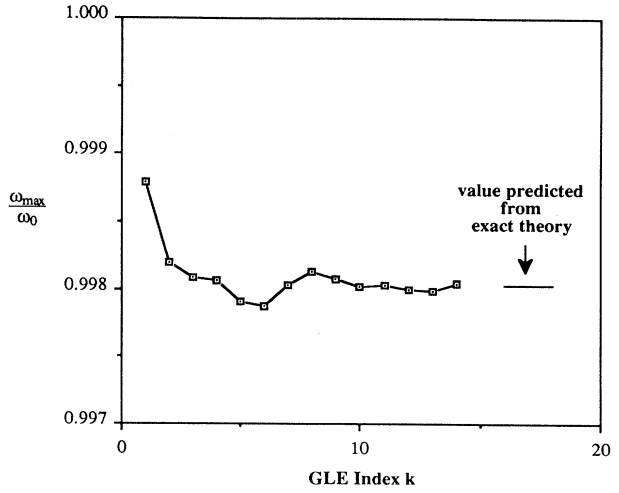

FIG. 2. Red-shifted oscillator frequency $\omega_{\max}$ normalized to ω_0 as a function of the GLE expansion index k for fixed values of the parameters ω_e and ω_c. Parameters are given in the text under set 1. Calculated to fourth order in the coupling constant.

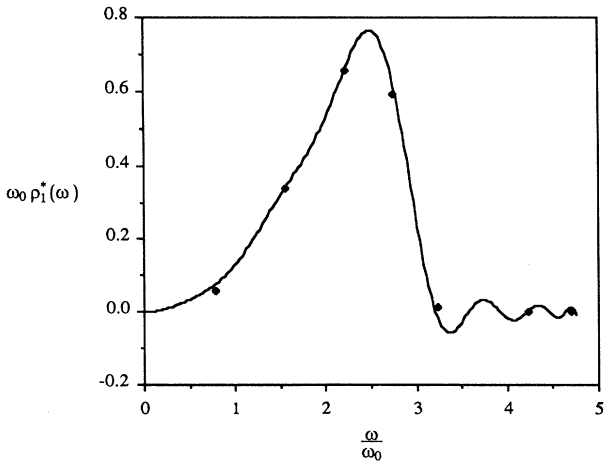

FIG. 1. Plot of the spectral density function $\rho_1^*(\omega)$ showing fit to the spectral density at the eigenfrequencies ω_1 through ω_N. The spectral density is required to be zero at $\omega = 0$. Parameters are given in the text under set 1. Calculated to fourth order in the coupling constant.

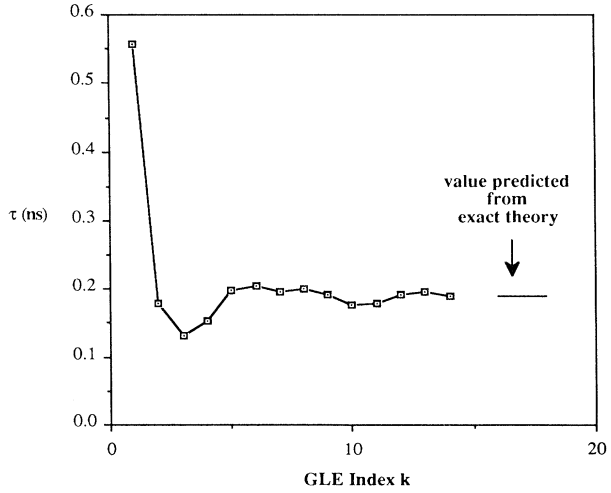

FIG. 3. Relaxation time τ as a function of GLE expansion index k for fixed values of the parameters ω_e and ω_c. Parameters are given in the text under set 1. Calculated to fourth order in the coupling constant.

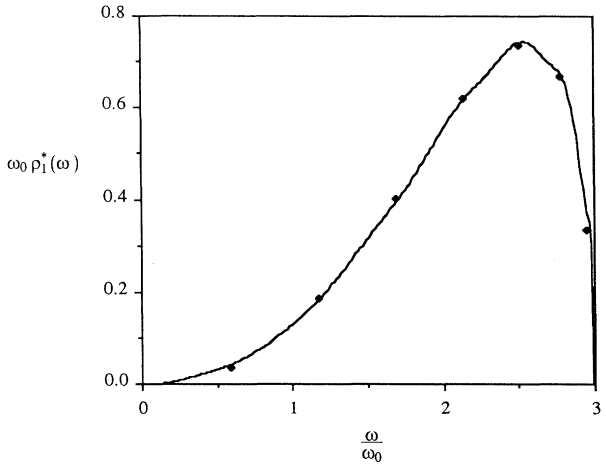

FIG. 4. Spectral density function $\rho_1^*(\omega)$ showing fit to the spectral density at the eigenfrequencies ω_1 through ω_N. Parameters are given in the text under set 2. Calculated to second order in the coupling constant.

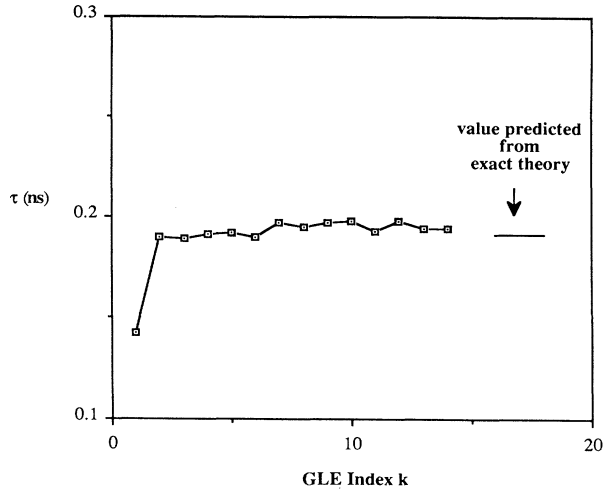

FIG. 6. Relaxation time τ as a function of GLE expansion index k for fixed values of the parameters ω_e and ω_c. Parameters are given in the text under set 2. Calculated to second order in the coupling constant.

for this set are $\hbar\omega_a = 60$ cm^{-1}, $\bar{\chi} = 0.3$ cm^{-1}, $T = 50$ K and $\hbar\omega_0 = 30$, 60, and 90 cm^{-1}. The calculations are carried out to fourth order in the coupling constant. The three spectral density functions are compared in Fig. 7. The important feature to note is that as the vibron oscillator frequency passes from below to above the upper limit ω_a of the phonon spectrum, the first bath spectral density $\rho_1^*(\omega)$ narrows and shifts to lower frequencies. We interpret this to mean that the vibron is increasingly decoupled from the phonon manifold, and increasingly dominates the first bath spectral density. This matter will be explored more fully in a subsequent paper which will examine the single oscillator Davydov and Takeno cases for the parameter regime of α-helix systems where $\omega_0 \gg \omega_a$. Figure 8 shows, as might be expected from the point of view described above, that the frequency $\omega_{\max}$ is less red-shifted as ω_0 increases from below to above ω_a. Figure 9 shows what is at first sight a rather surprising result. The converged relaxation time τ shows very little dependence on the vibron frequency, even though $\rho_1^*(\omega)$ increases in the vicinity of ω_0 and must therefore be compensated by a decrease in the coupling frequency ω_{c_i}. This somewhat counterintuitive effect is confirmed by the exact theory discussed in Sec. III leading to Eq. (84) for τ which is independent of ω_0.

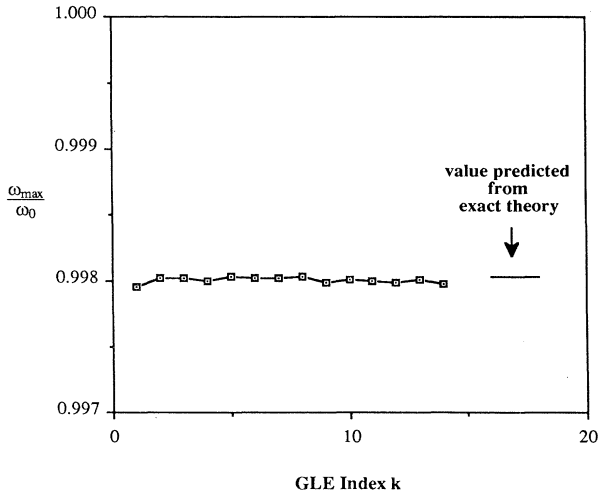

FIG. 5. Red-shifted oscillator frequency $\omega_{\max}$ normalized to ω_0 as a function of the GLE expansion index k for fixed values of the parameters ω_e and ω_c. Parameters are given in the text under set 2. Calculated to second order in the coupling constant.

Set 5: At very low temperatures MTGLE theory leads in some cases to the unexpected result that a band gap exists in the first bath spectral density extending from zero frequency to just above the vibron oscillator frequency. The vibron oscillator in such a case is predicted to have zero linewidth and infinite lifetime. This result is shown in Fig. 10 which is calculated to fourth order in the coupling constant for $\hbar\omega_a = 60$ cm^{-1}, $\hbar\omega_0 = 60$ cm^{-1}, $\bar{\chi} = 0.3$ cm^{-1}, and $T = 0$ K. At higher temperatures for these same parameters, the lower band edge of the first heat bath spectral density given by $\sqrt{\omega_e^2 - 2\omega_c^2}$ crosses below the red-shifted vibron oscillator frequency $\omega_{\max}$ at about 1.6 K as shown in Fig. 11. Above this temperature the vibron oscillator acquires a finite linewidth and lifetime, but results below 10 K converge more slowly than at higher temperatures.

For the parameter set where $\omega_0 \cong \omega_a/2$ the band gap edge occurs below ω_0 so that the vibron has a finite width and lifetime even at $T = 0$ K. Figure 12 shows the lower band edge of the first heat-bath spectral density versus

TABLE III. Comparison of second-order, fourth-order, and exact results for ω_{e_N} and ω_{c_N}. The parameters used are $\hbar\omega_a=60\ \mathrm{cm}^{-1}$, $\hbar\omega_0=60\ \mathrm{cm}^{-1}$, $\bar{\chi}=0.3\ \mathrm{cm}^{-1}$, and $T=0$ K.

N	Second order	$\frac{\omega_{e_N}^2}{\omega_0^2}$ Fourth order	Exact
0	0.999 685	0.999 685	0.999 685
1	2.704 267	2.703 511	2.703 511
2	2.561 617	2.580 306	2.580 301
3	2.539 516	3.116 442	3.118 803
4	2.539 829	5.655 815	5.697 940

N	Second order	$\frac{\omega_{c_N}^4}{\omega_0^4}$ Fourth order	Exact
1	0.000 573	0.000 573	0.000 573
2	0.491 299	0.497 103	0.497 101
3	0.528 460	0.627 270	0.627 413
4	0.534 417	2.719 056	2.740 082

temperature for $\hbar\omega_a=60\ \mathrm{cm}^{-1}$, $\hbar\omega_0=30\ \mathrm{cm}^{-1}$, and $\bar{\chi}=0.3\ \mathrm{cm}^{-1}$ calculated to fourth order in the coupling constant.

We interpret these results as follows. In the case of linear coupling the vibron will have zero width and infinite lifetime if its frequency ω_0 lies above the upper band edge ω_a of the phonon spectrum. In the nonlinear case a related effect occurs even when the vibron frequency is at or just below ω_a, and persists in its effects when ω_0 is as small as $\frac{1}{2}\omega_a$. This band gap effect is closely related to the anomalous time dependence of $\dot{\chi}(t)$ at low temperatures calculated in Sec. III from the exact theory, and will be examined more closely in Sec. V.

Set 6: Figures 13 and 14 are calculated to fourth order in the coupling constant for the parameter set $\hbar\omega_a=60\ \mathrm{cm}^{-1}$, $\hbar\omega_0=30\ \mathrm{cm}^{-1}$, and $\bar{\chi}=0.3\ \mathrm{cm}^{-1}$ and various temperatures. Figure 13 shows the reciprocal lifetime $1/\tau$ as a function of temperature. This reciprocal lifetime is linear in temperature as predicted by the exact theory and also agrees in magnitude with the exact theory as will be shown in Sec. V. Figure 14 shows the red-shifted vibron oscillator frequency $\omega_{\max}$ as a function of tempera-

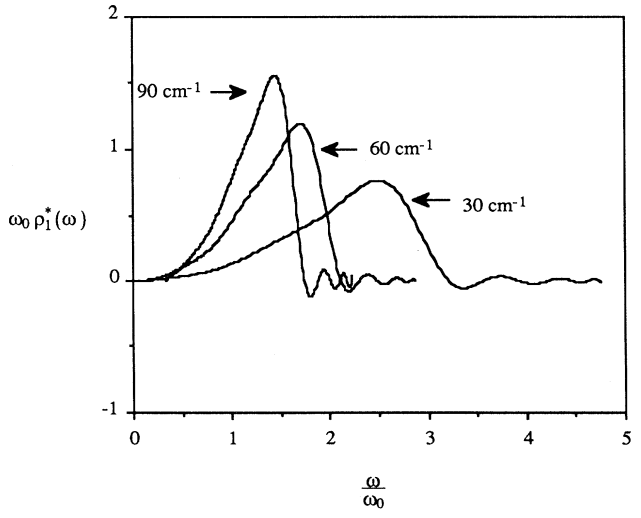

FIG. 7. Spectral density function $\rho_1^*(\omega)$ for three different values of the external oscillator frequency ω_0. The remaining parameters are given in the text for set 4. Calculated to fourth order in the coupling constant.

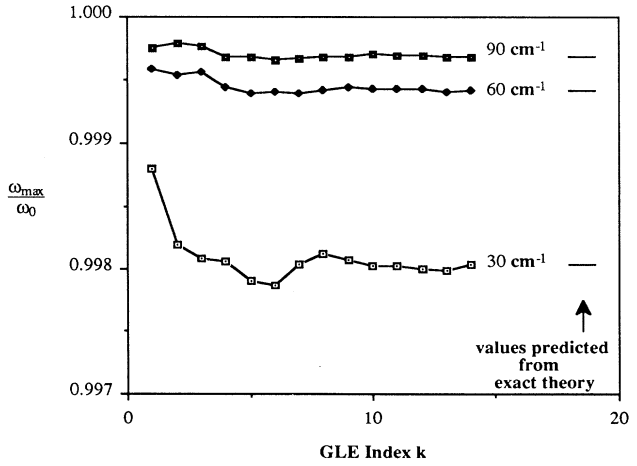

FIG. 8. Red-shifted oscillator frequency $\omega_{\max}$ normalized to ω_0 as a function of the GLE expansion index k for fixed values of the parameters ω_e and ω_c. Results are shown for three values of the vibron oscillator frequency ω_0. The remaining parameters are given in the text under set 4. Calculated to fourth order in the coupling constant.

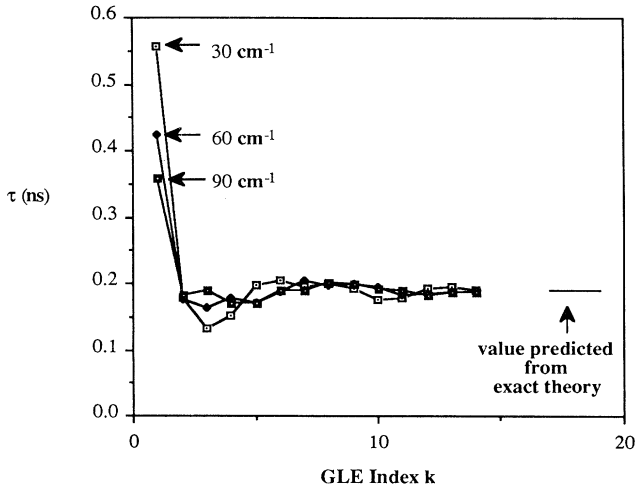

FIG. 9. Relaxation time τ as a function of GLE expansion index k for fixed values of the parameters ω_e and ω_c. Results are shown for three values of the vibron oscillator frequency ω_0. The remaining parameters are given in the text under set 4. Calculated to fourth order in the coupling constant.

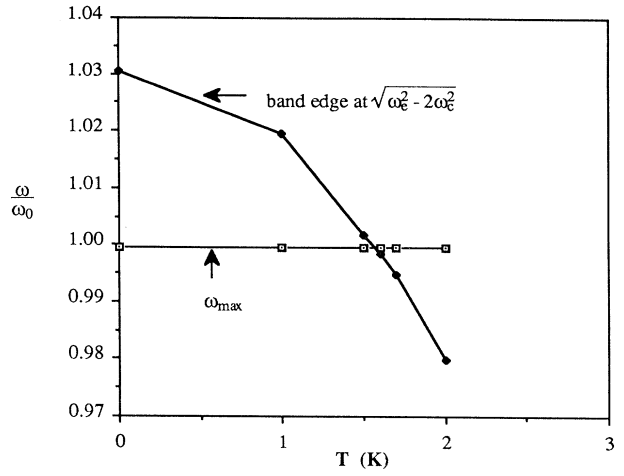

FIG. 11. Lower band edge of the first heat-bath spectral density plotted as a function of temperature for the parameter set $\hbar\omega_a = 60\ \text{cm}^{-1}$, $\hbar\omega_0 = 60\ \text{cm}^{-1}$, and $\bar{\chi} = 0.3\ \text{cm}^{-1}$. Calculated to fourth order in the coupling constant. The lower band edge crosses the red-shifted vibron oscillator frequency $\omega_{\max}$ at about 1.6 K.

ture. In view of the expanded vertical scale, the red-shifts are very small ranging up to 1%. Nevertheless the temperature dependence of the red-shift given by MTGLE theory is in close agreement with results predicted from the exact theory as will be seen in Sec. V. The close agreement of lifetime and red-shift as a function of temperature with the exact theory is a very severe test of the accuracy of MTGLE theory in the time regime for which it is valid.

Set 7: Figure 15 presents a summary of results for relaxation time τ as a function of temperature calculated to fourth order in the coupling constant for the parameters

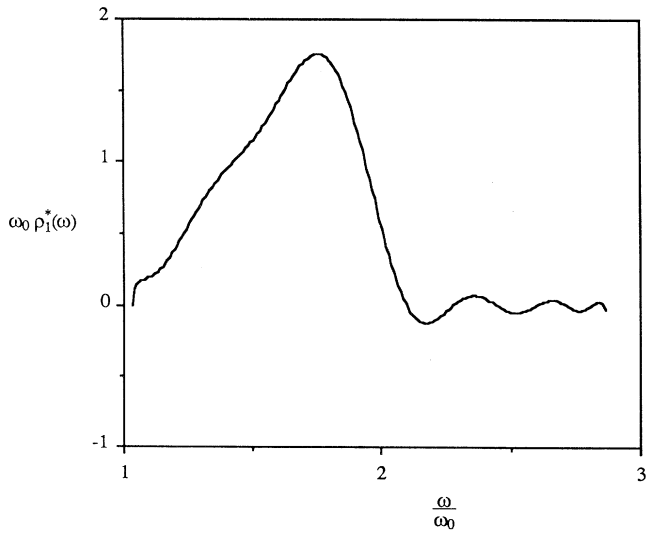

FIG. 10. Plot of the spectral density function $\rho_1^*(\omega)$ at $T=0$ K for the parameter set $\hbar\omega_a = 60\ \text{cm}^{-1}$, $\hbar\omega_0 = 60\ \text{cm}^{-1}$, and $\bar{\chi} = 0.3\ \text{cm}^{-1}$ calculated to fourth order in the coupling constant. The lower band edge of the spectral density in this case lies just above the vibron oscillatory frequency ω_0.

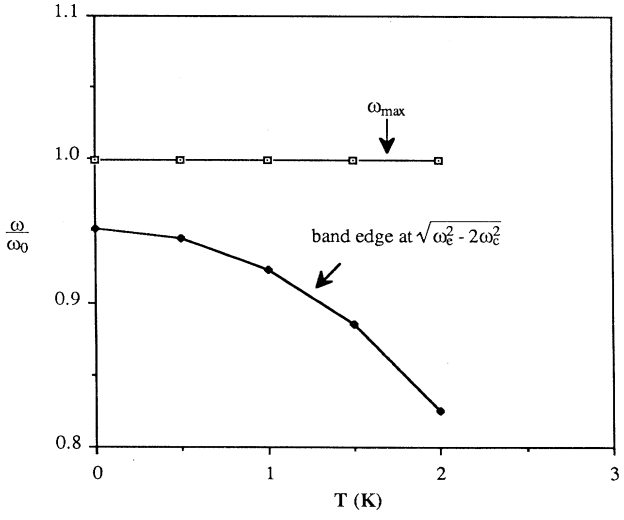

FIG. 12. Lower band edge of the first heat-bath spectral density plotted as a function of temperature for the parameter set $\hbar\omega_a = 60\ \text{cm}^{-1}$, $\hbar\omega_0 = 30\ \text{cm}^{-1}$, and $\bar{\chi} = 0.3\ \text{cm}^{-1}$. Calculated to fourth order in the coupling constant. The lower band edge always lies below the red-shifted vibron oscillator frequency $\omega_{\max}$.

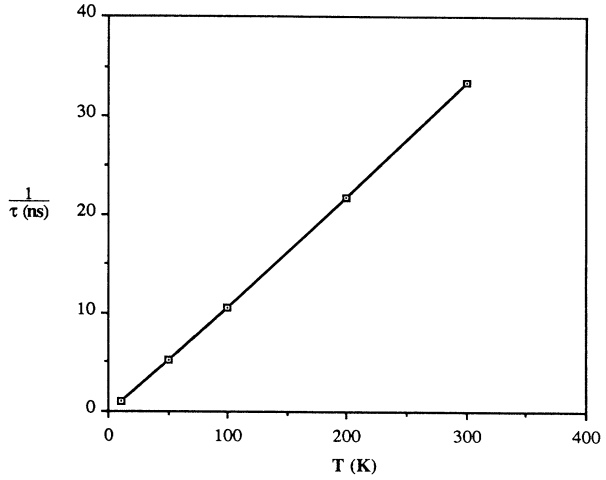

FIG. 13. Reciprocal $1/\tau$ of the relaxation time τ plotted as a function of temperature for the parameters under set 4. Calculated to fourth order in the coupling constant.

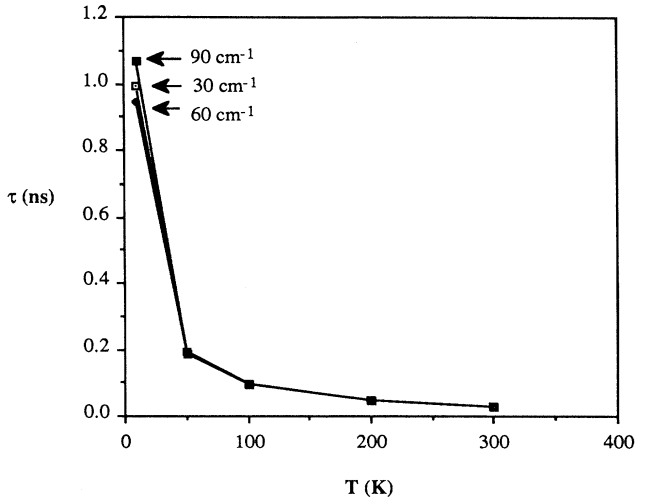

FIG. 15. Reciprocal $1/\tau$ of the relaxation time τ plotted as a function of temperature for the parameters under set 7. Calculated to fourth order in the coupling constant. Except at the lowest temperatures, the relaxation time is independent of the vibron oscillator frequency ω_0.

$\hbar\omega_a = 60$ cm^{-1}, $\bar{\chi} = 0.3$ cm^{-1} and $\hbar\omega_0 = 30$, 60, and 90 cm^{-1}. It will be noted that the relaxation time, except for the lowest temperatures, is independent of the vibron oscillator frequency ω_0 as predicted by the exact theory.

Set 8: Figure 16 presents a summary of results for the red-shifted oscillator frequency $\omega_{\max}$ as a function of temperature calculated to fourth order in the coupling constant for the parameters $\hbar\omega_a = 60$ cm^{-1}, $\bar{\chi} = 0.3$ cm^{-1} and $\hbar\omega_0 = 30$, 60, and 90 cm^{-1}. As mentioned in connection with set 4, $\omega_{\max}$ is less red-shifted as ω_0 increases from below to above the upper limit of the phonon band ω_a, and this result holds for all temperatures. These results for $\omega_{\max}$ as a function of temperature for different values of ω_0 are also in excellent agreement with results predicted from the exact theory for the time regime in which MTGLE theory is valid.

Set 9: This final set of results, similar to set 1, comprises three figures intended to show a typical set of results at a larger nonlinear coupling constant $\bar{\chi} = 1.0$ cm^{-1}. The other parameters are equal to those in set 1, $\hbar\omega_a = 60$ cm^{-1}, $\hbar\omega_0 = 30$ cm^{-1}, $T = 50$ K, and the calculation is done to fourth order in the coupling constant. Since all nonlinear effects vary as $\bar{\chi}^2$, nonlinear effects in this set of results are more than 10 times greater than in set 1, but well-converged results are still achieved. The

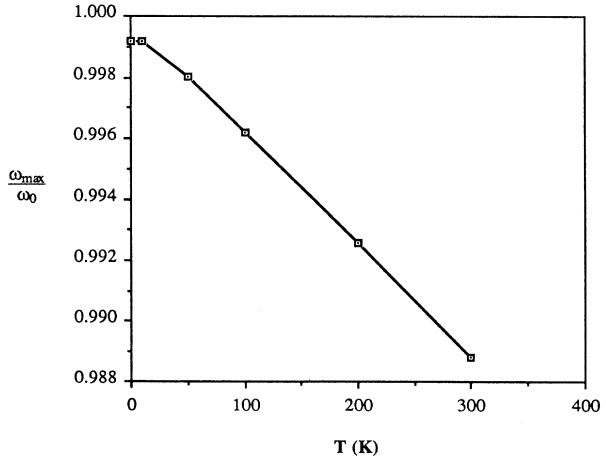

FIG. 14. Red-shifted oscillator frequency $\omega_{\max}$ as a function of temperature for the parameters given in the text under set 6. Calculated to fourth order in the coupling constant.

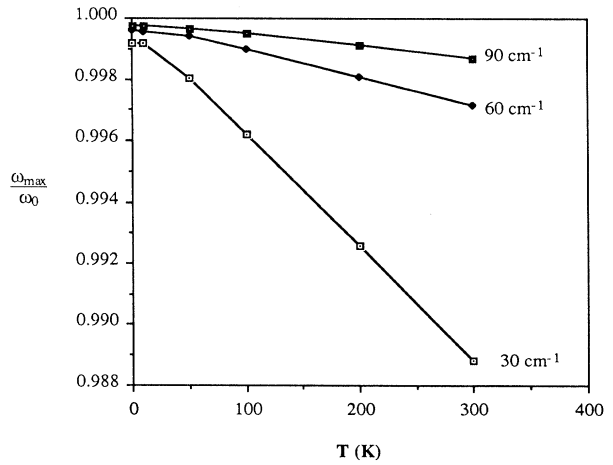

FIG. 16. Red-shifted oscillator frequency $\omega_{\max}$ as a function of temperature for the parameters given in the text under set 8. Calculated to fourth order in the coupling constant.

TABLE IV. Eigenfrequencies and spectral weights of first heat bath at fourth order. The parameters used are $\hbar\omega_a = 60$ cm^{-1}, $\hbar\omega_0 = 30$ cm^{-1}, $\bar{\chi} = 1.0$ cm^{-1}, and $T = 50$ K.

n	ω_n/ω_0	$\lvert T_{n1}\rvert^2$
1	0.849 851	0.081 954
2	1.613 141	0.266 327
3	2.294 666	0.411 813
4	2.808 672	0.232 199
5	3.670 696	0.006 353
6	4.310 365	0.001 233
7	4.743 146	0.000 120

eigenfrequencies and spectral weights listed in Table IV differ in detail from the corresponding quantities listed in Table II. Nevertheless, remarkably enough, the first heat-bath spectral densities shown in Figs. 1, 4, and 17 are nearly identical. This reflects the fact that the first heat-bath spectral density is largely independent of the strength of the nonlinear coupling parameter in the range we have studied. The converged frequency of the external oscillator shown in Fig. 18 is considerably more red-shifted than the red-shifted frequency $\omega_{\max}$ shown in Fig. 2. The effect of increased nonlinear coupling on the relaxation time τ should go as $\bar{\chi}^{-2}$ according to the exact theory result given in Eq. (84). This agrees almost exactly with the value $\tau = 0.0155$ obtained from Fig. 19 and $\tau = 0.19$ obtained from Fig. 3.

V. COMPARISON OF QUANTUM MTGLE THEORY WITH EXACT THEORY

In the preceding section results were presented for the red-shifted frequency $\omega_{\max}$ of the vibron oscillator and its

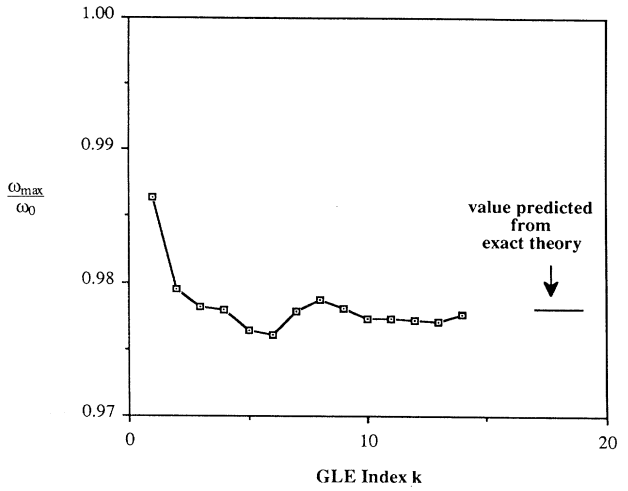

FIG. 18. Red-shifted oscillator frequency $\omega_{\max}$ normalized to ω_0 as a function of the GLE expansion index k for fixed values of the parameters ω_e and ω_c. Parameters are given in the text under set 9. Calculated to fourth order in the coupling constant.

lifetime τ based on the MTGLE theory developed in Sec. II. Confidence in the MTGLE theory within its valid time domain is based on the general considerations discussed in Sec. II, and on the rapid convergence of $\omega_{\max}$ and τ as a function of the GLE expansion index k demonstrated by the calculated results of Sec. IV. Further confidence in the MTGLE theory within its valid time domain is provided by its close agreement with exact theory as described below.

We first look in greater detail at the nature of the

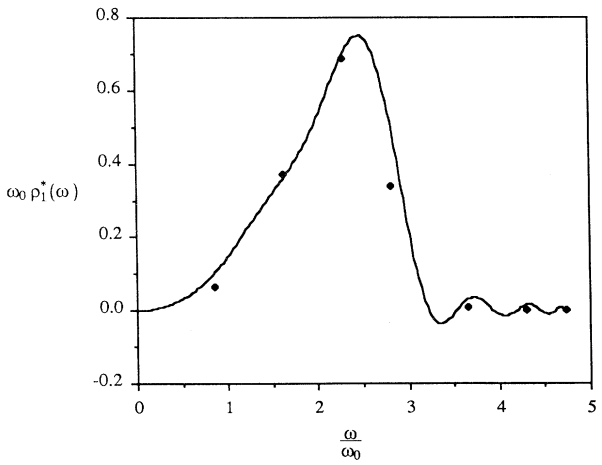

FIG. 17. Plot of the spectral density function $\rho_1^*(\omega)$ showing fit to the spectral density at the eigenfrequencies ω_1 through ω_N. The spectral density is required to be zero at $\omega = 0$. Parameters are given in the text under set 9. Calculated to fourth order in the coupling constant.

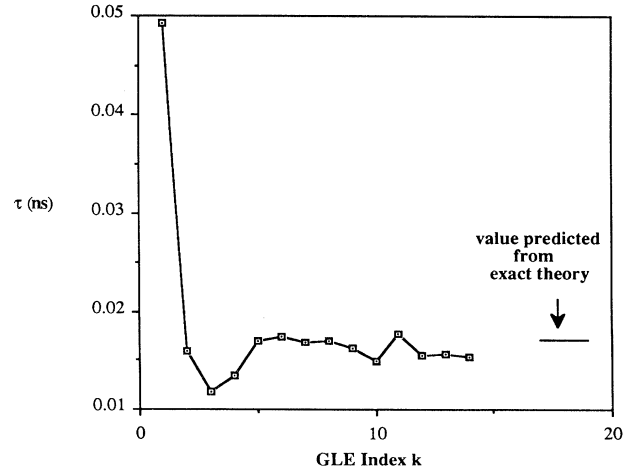

FIG. 19. Relaxation time τ as a function of GLE expansion index k for fixed values of the parameters ω_e and ω_c. Parameters are given in the text under set 9. Calculated to fourth order in the coupling constant.

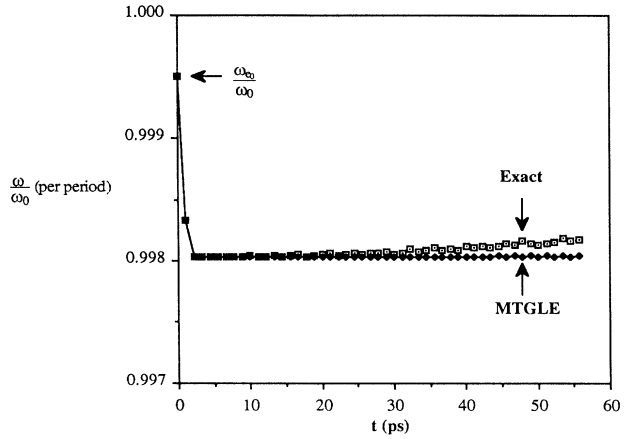

FIG. 20. Frequency per period of $\chi(t)$ calculated from exact theory and from MTGLE theory. The initial frequency at $t=0$ is taken to be the Einstein frequency. Parameters of the calculation are given in the text.

agreement between MTGLE theory and the exact theory. Figure 20 shows the frequency per period of $\dot{\chi}(t)$ calculated as a function of time from the exact theory according to Eq. (77), and from the MTGLE theory using Eqs. (22) and (36). (In each case successive maxima were found, the time difference Δ determined, and the radian frequency per period computed as $2\pi/\Delta$.) The parameters chosen for this illustrative case are the same as those of set 1 in Sec. IV. In Fig. 20 we have also included at $t=0$ a point for the exact Einstein frequency ω_{e_0} as defined by Eq. (41a). For this case $\omega_{e_0}/\omega_0=0.999507$. In examining Fig. 20 we see that after a very short transient of order two cycles of the fundamental frequency ω_0, the frequency per period calculated from the exact theory stabilizes at the frequency given in Eq. (88) and then gradually increases after about 30 ps. This increase is understood by appeal to Eq. (86). We see that the argument of the cosine in the numerator is being continually phase shifted as time increases. Thus, the simple short-time formula in Eq. (88) becomes invalid after about 30 ps.

In Fig. 20 the frequency per period calculated from the MTGLE theory traces out exactly the same transient as the exact theory and then stabilizes indefinitely at the frequency given by Eq. (88). Significant deviation of the exact theory and MTGLE theory occurs at about 40 ps which represents the limit of validity in this case of the MTGLE calculation of $\dot{\chi}(t)$. Although this breakpoint of 40 ps is sufficiently long enough to allow for about 40 vibrational periods, it is short enough relative to the 1-ns phase-shift effect that the short-time frequency formula in Eq. (88) accurately predicts the $\omega_{\max}$ obtained from MTGLE theory. This predicted value of $\omega_{\max}$ is shown in Figs. 2, 5, 8, and 18. A more complete comparison is given in Table V which shows excellent agreement between the results of Eq. (88) and MTGLE theory over a wide range of temperatures and values of ω_0. The agreement extends to much larger coupling constants $\bar{\chi}$ as shown in Fig. 18.

The time limit of 40 ps noted in Fig. 20 has an interesting implication. For this case, using the parameters of set 1 in Sec. IV, Eq. (53) becomes $t=1.047\times10^{-13}$ k. This means that the MTGLE calculation of $\omega_{\max}$ would not change if the GLE expansion index were extended to $k=380$. This helps to explain why $\omega_{\max}/\omega_0$ in Figs. 2, 5, and 18 converges rapidly to its final value.

This same situation can be looked at from an even more interesting perspective. Starting with the exact expression for $\dot{\chi}(t)$ given by Eq. (77) we can calculate the real and imaginary parts of $\chi(i\omega)$. Then, using Eq. (26) we can obtain real and imaginary parts of $\omega_{c_1}^4\hat{\theta}_1(i\omega)$ and therefore exact values for $I(\omega)$ and $R(\omega)$ given by Eqs. (35) and $\rho_1(\omega)$ given by Eq. (33). The result of this calculation for $\omega_0\rho_1(\omega)$ near $\omega=\omega_{\max}$ using the parameters of Sec. IV, Set 1, is shown in Fig. 21 superimposed on the MTGLE calculation of $\omega_0\rho_1^*(\omega)$ shown in Fig. 1. The vertical and horizontal scales in Fig. 21 have been expanded to bring out the very localized nature of the difference $\Delta\rho_1(\omega)$ between the exact and MTGLE values of $\rho_1(\omega)$. The difference $\Delta\rho_1(\omega)$ is clearly a result of large-k Fourier components in the Fourier sine series in Eq. (60); that is, if $\Delta\rho_1(\omega)$ were to be represented by the MTGLE series

$$\Delta\rho_1(\omega)=\frac{2\omega}{\pi\omega_c^2}\sum_k\gamma_k\sin k\phi(\omega)\ , \tag{89}$$

which is similar to Eq. (62), then very large-k values would necessarily be required in the sum to represent the spike in Fig. 21. These values would in fact peak around $k=\pi\omega_c\tau/4$, and through Eq. (53) correspond to a time $t=\pi/4(\omega_e/\omega_c)\tau$. This is consistent with the notion that

TABLE V. Comparison of MTGLE and analytic results [Eq. (101)] for $\omega_{\max}/\omega_0$ at several values of the vibron frequency ω_0 and as a function of temperature.

$\hbar\omega_0$	30 cm^{-1}		60 cm^{-1}		90 cm^{-1}	
T (K)	MTGLE	Exact	MTGLE	Exact	MTGLE	Exact
0	0.999 203	0.999 200	0.999 605	0.999 600	0.999 736	0.999 733
10	0.999 178	0.999 178	0.999 589	0.999 600	0.999 740	0.999 733
50	0.998 036	0.998 032	0.999 418	0.999 427	0.999 681	0.999 690
100	0.996 200	0.996 234	0.999 000	0.999 016	0.999 518	0.999532
200	0.992 558	0.992 555	0.998 085	0.998 118	0.999 122	0.999 148
300	0.988 807	0.988 856	0.997 151	0.997 200	0.998 709	0.998 745

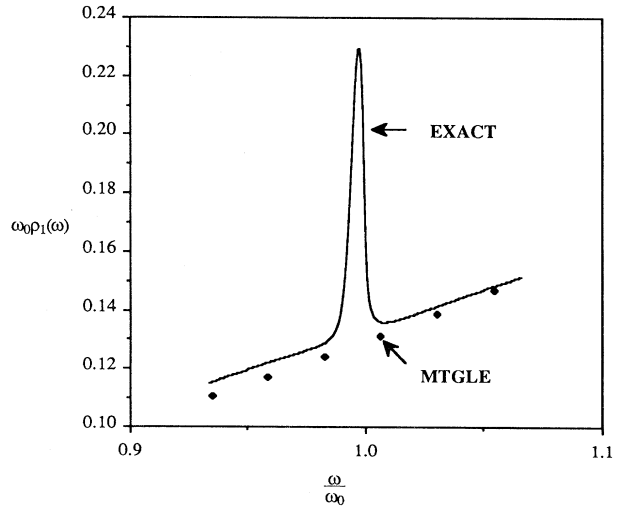

FIG. 21. First heat-bath spectral density near $\omega=\omega_{\max}$ for exact theory and MTGLE theory. Parameters used are those of set 1.

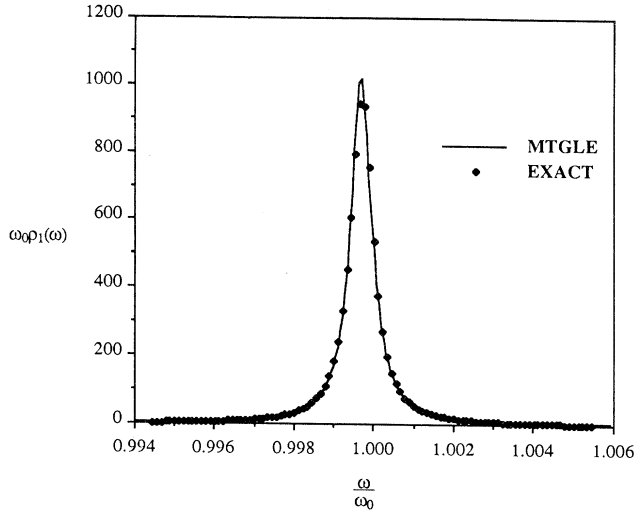

FIG. 23. Spectral density of the time-correlation function $\dot{\chi}(t)$ computed via exact theory and MTGLE theory. Parameters are those of set 1 with $\hbar\omega_0=90\ \mathrm{cm}^{-1}$.

longer times produce finer resolution. The effect of the high-resolution spike near $\omega=\omega_{\max}$ in the exact first bath spectral density on the spectral density $\rho(\omega)$ of $\dot{\chi}(t)$ is shown in Fig. 22. We see that it produces a broadening and reduction of the red-shift of the exact line shape relative to the MTGLE line shape. Although this long-time or high-resolution broadening effect is significant in this case, it is not apparent in other regions of parameter space. We show in Fig. 23 a comparison of $\rho(\omega)$ for the exact and MTGLE theories at $\hbar\omega_0=90\ \mathrm{cm}^{-1}$ with the other parameters fixed to those of set 1. Here we find essentially perfect agreement. The conclusion to be drawn is that MTGLE has a domain of validity in time which for some parameter sets is sufficient to produce the exact spectral density $\rho(\omega)$ but for others is less than the time required to sample high-resolution contributions.

As a follow-on to the plot in Fig. 21, we have extended the frequency range and show in Fig. 24 a comparison between the MTGLE bath spectral density $\omega_0\rho_1^*(\omega)$ and the exact bath spectral density $\omega_0\rho_1(\omega)$. The values for $\omega_0\rho_1(\omega)$ are computed as described above using a Simpson's rule evaluation with 50 000 time points out to 2 ns. We find overall good agreement between the two approaches with excellent agreement at lower frequencies aside from the narrow spike near $\omega=\omega_{\max}$. As mentioned

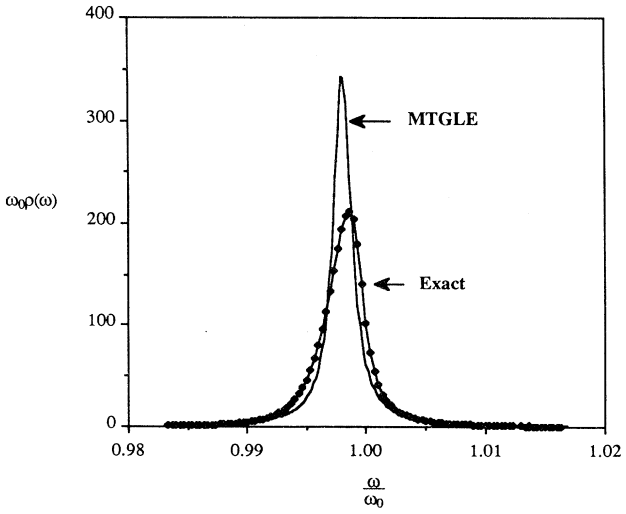

FIG. 22. Spectral density of the time-correlation function $\dot{\chi}(t)$ computed via exact theory and MTGLE theory. Parameters are those of set 1.

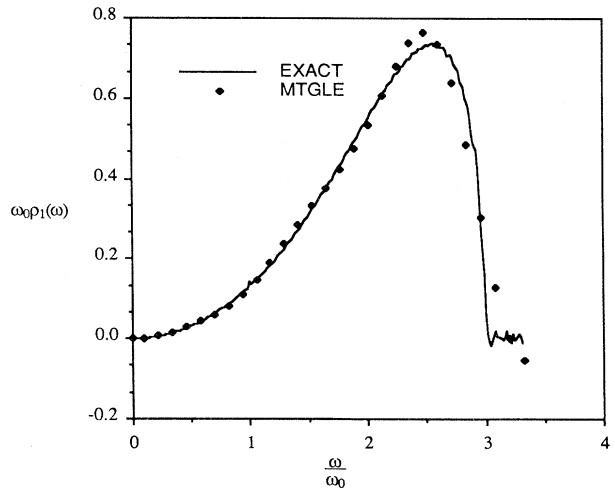

FIG. 24. First heat-bath spectral density for exact theory and MTGLE theory. Parameters are those of set 1.

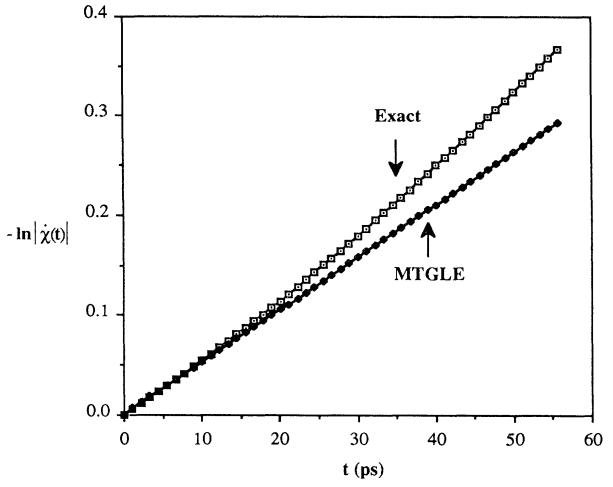

FIG. 25. Decay of modulus of $\dot{\chi}(t)$ calculated from the exact theory and from MTGLE theory and plotted as $-\ln|\dot{\chi}(t)|$. The MTGLE result is essentially a straight line conveying the exponential decay. Parameters of the calculation are $\hbar\omega_0=30$ cm^{-1}, $\hbar\omega_a=60$ cm^{-1}, $\bar{\gamma}=0.3$ cm^{-1}, and $T=50$ K.

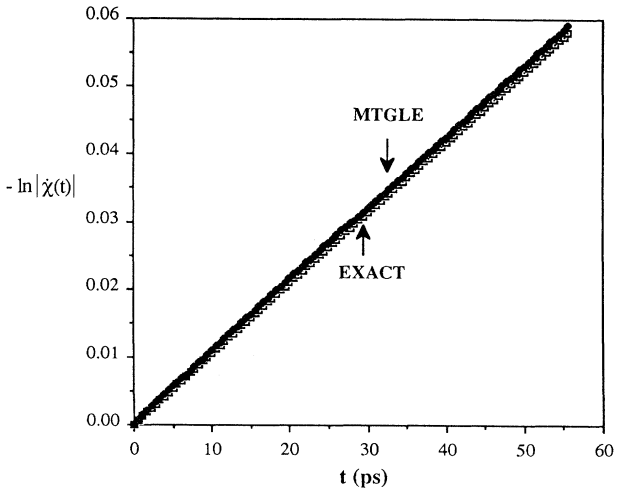

FIG. 26. $\ln|\dot{\chi}(t)|$ as a function of time for $T=10$ K computed from exact theory and MTGLE theory. Other parameters are $\hbar\omega_0=60$ cm^{-1}, $\hbar\omega_a=60$ cm^{-1}, and $\bar{\gamma}=0.3$ cm^{-1}.

in Sec. II, this demonstrates that our fitting procedure using GLE functions is satisfactory.

A similar picture emerges in making comparisons of the modulus (defined as the locus of maximum points) of $\dot{\chi}(t)$, denoted as $|\dot{\chi}(t)|$, calculated as a function of time from the exact and MTGLE theories. In Fig. 25 we present results computed by finding successive maxima as described above. Because of normalization, both theories start at amplitude unity. We plot the results as $\ln|\dot{\chi}(t)|$ so that simple exponential decay produces a straight line. As expected, the MTGLE curve is essentially linear. The exact curve on the other hand follows the MTGLE curve accurately up to about 30 ps and then deviates. This deviation again has its origin in Eqs. (82) and (86) which represent the long-time behavior of the exponential and prefactor terms appearing in the exact expression in Eq. (77). We have verified that these expressions are valid after only 1–2 ps for the parameters specified above. Examination of these equations, particularly the denominator of Eq. (86), shows that there is very long time structure over and above simple exponential decay which leads to the nonlinear behavior of the exact theory in Fig. 25. Since the MTGLE theory follows exponential decay, since it accurately agrees with the exact theory up to about 30 ps, and since the very long-time shift effects should not be revealed in the first 30 ps, one expects that the exact lifetime formula in Eq. (84) which is extracted from the purely exponential part of $\dot{\chi}(t)$ will be in excellent agreement with MTGLE theory. This agreement is shown in Table VI. It is furthermore significant that the MTGLE theory agrees with the exact theory in that the relaxation time is independent of the vibron oscillator frequency ω_0. The only significant discrepancy is at 10 K and is related to the observation made in Sec. IV under set 5 that the calculation of τ converges more slowly as a function of the GLE expansion index k at lower temperatures. Even here, however, the exact and MTGLE results agree within 1%. Furthermore, $\ln|\dot{\chi}(t)|$ in both cases is a linear function of time indicating exponential decay as shown in Fig. 26, and agreement at this level extends out to well beyond 40 ps.

As the temperature decreases further toward the crossover point of 1.6 K shown in Fig. 11, the discrepancies between the exact and MTGLE theories become more marked. In Fig. 27 $\ln|\dot{\chi}(t)|$ is shown as a function of time at 1.6 K just above the crossover point. At this tempera-

TABLE VI. Comparison of MTGLE and exact lifetimes in nanoseconds as a function of vibron frequency ω_0 and temperature.

$\hbar\omega_0$	30 cm^{-1}	60 cm^{-1}	90 cm^{-1}	
T (K)				Exact
10	0.993	0.944	1.068	0.955
50	0.191	0.189	0.189	0.191
100	0.094	0.094	0.094	0.095
200	0.046	0.047	0.047	0.048
300	0.030	0.031	0.031	0.032

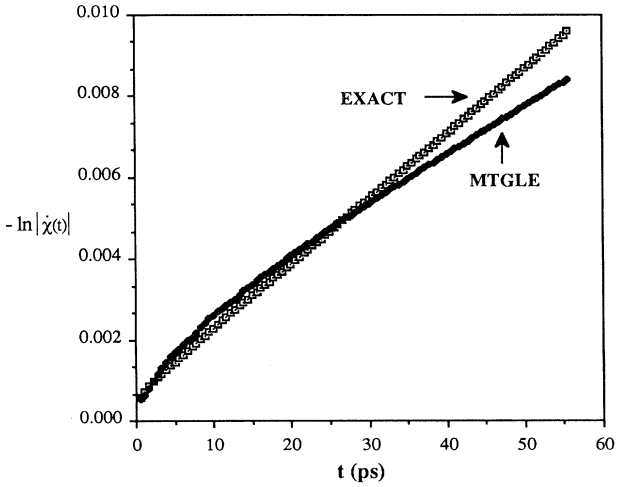

FIG. 27. $\ln|\dot{\chi}(t)|$ as a function of time for $T=1.6$ K computed from exact theory and MTGLE theory. Other parameters as in Fig. 26.

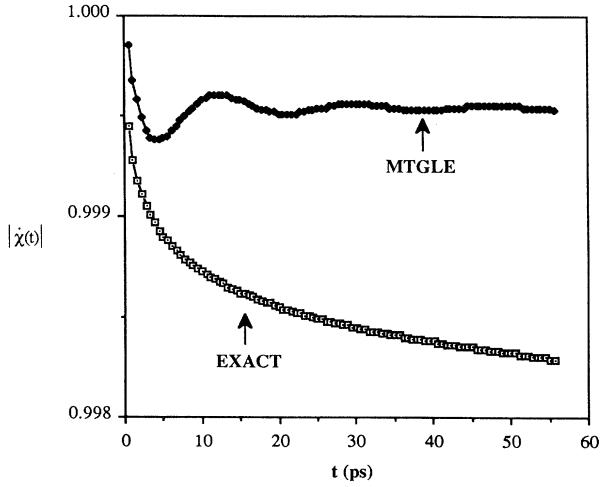

FIG. 29. $|\dot{\chi}(t)|$ as a function of time for $T=0$ K computed from exact theory and MTGLE theory. Other parameters as in Fig. 26.

ture $\ln|\dot{\chi}(t)|$ is still a linear function of time for the exact theory, but is no longer so for the MTGLE theory. Some differences between the MTGLE and exact theories appear at times as short as 5 ps where the MTGLE result rises above the exact result, and again beyond 30 ps where the MTGLE result drops below the exact result. Even this close to the crossover point the exact result and MTGLE result still agree to within 10% out to 40 ps.

At 1.5 K (below the crossover point) the differences become much larger as two effects set in. First, $|\dot{\chi}(t)|$ calculated from MTGLE theory develops an infinite lifetime as $\omega_{\max}$ in Fig. 11 drops below the band edge $\sqrt{\omega_e^2-2\omega_c^2}$. The effect of this is shown in Fig. 28 where $|\dot{\chi}(t)|$ is shown as a function time at 1.5 K. After an initial decline extending out to about 30 ps it levels off, and if carried further would take on a constant value corresponding to infinite lifetime. A second effect is seen in the exact calculation of $|\dot{\chi}(t)|$. The quantum fluctuation decay time scale given by $2\pi t=\hbar\beta$ now extends out to 0.8 ps so that $|\dot{\chi}(t)|$ first declines as a small power of time before resuming an exponential decay. As a result the MTGLE theory has no extended region of agreement with the exact theory.

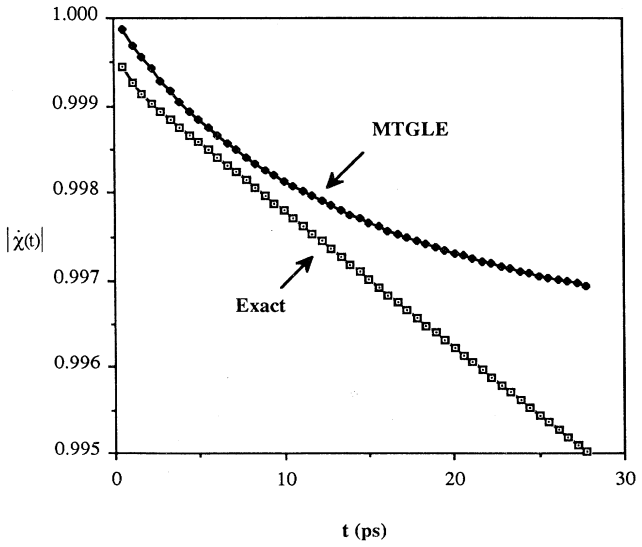

FIG. 28. $|\dot{\chi}(t)|$ as a function of time for $T=1.5$ K computed from exact theory and MTGLE theory. Other parameters as in Fig. 26.

At 0 K the discrepancy between the calculation of $|\dot{\chi}(t)|$ by the exact theory and the MTGLE theory becomes large as illustrated in Fig. 29. The MTGLE theory continues to predict an infinite lifetime corresponding to the leveling off of the upper curve in the figure beyond 30 ps. The quantum fluctuation time scale now extends to infinity so that the lower curve represents the small power-law decay given by Eq. (85).

The series of very low temperature results given in Figs. 26, 27, and 28 seem to relate the emergence of an infinite lifetime in the MTGLE theory with the emergence of a nonexponential decay in the exact theory. We have not yet attempted to establish such a relationship between the very low temperature predictions of the two theories and will leave that to a subsequent publication.

VI. SUMMARY AND CONCLUSIONS

Molecular crystals comprised of two or more nonlinearly coupled vibrational systems introduce an important new class of many-body problems into the physics and chemistry of the solid state. Much of the recent work in the area has focused on long, pseudo-one-dimensional chains of molecules which support a system of acoustic phonons nonlinearly coupled to high-frequency optical vibrons. The interest in such systems

stems largely from their potential for forming long-lived localized states with at least some of the properties of solitons. If the lifetimes of such states are sufficiently long, they can play a significant role in the thermodynamics of the crystals and may represent an important mechanism of energy transport. Theoretical and experimental interest has therefore focused on the lifetimes of localized excitations.

Coupled vibrational systems of this sort are almost universally described by the so-called Takeno Hamiltonian. This Hamiltonian presents such difficulties that no satisfactory exact or approximate solutions have yet been found. Approximate methods of solution abound, however, with little understanding of their range of validity, and many of these are mentioned in the Introduction. In some cases the Hamiltonian is truncated so as to preserve quanta in the vibron system. In our opinion this approximation, the so-called Davydov Hamiltonian, omits very important physics from the problem. In other cases a solution is approximated by adopting a product wave function. This so-called Davydov ansatz has been extensively criticized in the literature as a serious oversimplification.

In this paper we have begun the process of bringing to bear on these problems the methods of MTGLE theory. MTGLE theory does not require adopting either the Davydov Hamiltonian or Davydov ansatz but works directly by calculating the time-correlation function $\dot{\chi}(t)$ of a specified excitation from a large number of moments of the exact spectral density function $\rho(\omega)$ obtained from the Hamiltonian equations of motion. Although the theory is basically analytical, calculations of the moments and $\dot{\chi}(t)$ as well as the spectral density $\rho(\omega)$ both requires and is made possible by large-scale computation. In this first paper we have opted to examine the very simple problem of a single-vibron oscillator coupled nonlinearly to an acoustic phonon manifold because this Hamiltonian can be diagonalized exactly by a canonical transformation as shown in Sec. III. As a consequence, the time dependence of the time-correlation function $\dot{\chi}(t)$ can be obtained explicitly. It thereby allows direct comparison with the results of MTGLE theory and verification of the time domain of validity of MTGLE theory.

MTGLE theory proceeds by defining a hierarchy of heat-bath functions $\dot{\theta}_m(t)$ whose Laplace transforms satisfy an infinitely continued fraction. In Sec. II we have outlined a new approach to MTGLE theory that provides an optimized fit $\rho_1^*(\omega)$ to the discrete spectral density $\tilde{\rho}_1(\omega)$ of the first heat bath $\dot{\theta}_1(t)$ obtained by calculating 15 moments of $\rho(\omega)$. Knowledge of the first heat-bath spectral density allows us to make calculations of the red-shift of the vibron and its lifetime that are highly accurate within the valid time domain of the MTGLE theory.

In Sec. III we have outlined the exact theory of the nonlinearly coupled single-vibron oscillator which will be discussed in more detail in a forthcoming paper. This exact theory has been discussed before in the literature, but we have had to carry the theory much further, and make explicit computer calculations in order to make comparisons with MTGLE theory. One unexpected result of this extension of the exact theory is the discovery that the correlation function $\dot{\chi}(t)$ has a slow power-law decay at temperatures near absolute zero.

In Sec. IV and Figs. 1–19 we show a selection of results calculated by MTGLE theory for various values of the vibron frequency ω_0, the upper band edge of the phonon spectrum ω_a, the nonlinear coupling constant $\bar{\chi}$, and the temperature T. With so many primary parameters the results are necessarily representative only. These include principally the first heat-bath spectral density $\rho_1^*(\omega)$ showing its fit to the discrete spectral density obtained for a finite number of moments; curves showing rapid convergence of the red-shifted vibron frequency $\omega_{\max}$ with increasing number of moments; and similar curves for the decay constant τ.

In Sec. V we have compared the MTGLE theory with the results of the exact theory and found complete agreement in nearly all cases for the red-shifted vibron oscillator frequency $\omega_{\max}$ and the decay time τ within the valid time domain of the MTGLE theory. The only exception is below 2 K where the MTGLE theory begins to predict anonamously long lifetimes, culminating in infinite lifetimes for temperatures below 1.5 K with the vibron oscillator frequency near the upper band edge of the phonon spectrum. In the same region the exact theory predicts a transition from exponential decay to small power-law decay. We have not yet attempted to establish a direct connection between these two events.

The time domain of validity of MTGLE theory is in principle limited by the number of moments of the spectral density that can be accurately calculated. In practical terms this means that MTGLE theory will not include high-resolution effects. The degree to which this omission limits MTGLE theory and its ability to represent the spectral density $\rho(\omega)$ of $\dot{\chi}(t)$ is determined by the number of moments computed and the parameter values of the particular Hamiltonian system studied. For the present case of the single-vibron oscillator Davydov Hamiltonian, we have found that the parameter regime in which the vibron oscillator frequency ω_0 is on the order of one-half of the maximum phonon frequency ω_a is a regime in which high-resolution effects contribute and lead to a broadening of $\rho(\omega)$ relative to its MTGLE approximation. On the other hand this broadening does not affect the exponential lifetime factor τ which is well determined by MTGLE. Furthermore, as ω_0 is increased, the high-resolution effect goes away and $\rho(\omega)$ computed by MTGLE theory and exact theory come into excellent agreement. With the caveat that very high-resolution structure in the spectral density is omitted we conclude that the version of MTGLE theory presented herein is well suited to the study of local excitations in condensed matter systems and is capable of yielding both red shifts and lifetimes as a function of temperature.

ACKNOWLEDGMENTS

We thank J. D. Doll, A. Migliori, and L. R. Pratt for many fruitful discussions. Funding from the Los Alamos Center for Materials Science and the Los Alamos Internal Supporting Research and Development Program is gratefully acknowledged.

APPENDIX: CALCULATION OF TIME DERIVATIVES OF $\dot{\chi}(t)$

Generally speaking, the computation of the short-time derivatives (or spectral moments) of $\dot{\chi}(t)$ in Eq. (18) is the difficult step in making use of MTGLE theory. In the present case $\dot{\chi}(t)$ is known exactly through Eq. (77) and the time derivatives are immediately accessible. In subsequent papers which are anticipated in the Introduction we will not be able to compute the derivatives to higher than fourth order in the parameter σ_k. For this reason it is important to use the exact solution in Eq. (77) to compute MTGLE results as a function of powers of σ_k in order to demonstrate that higher than fourth order is unimportant in the parameter regime studied herein. Since $\dot{\chi}(t)$ manifestly depends on even powers of σ_k we have chosen to obtain results from the time derivatives computed to second order, fourth order, and exactly in σ_k.

Before proceeding with this expansion in σ_k we define two sets of auxiliary parameters:

$$f_n=\sum_k \frac{\sigma_k^2}{\omega_k^2}\left[\frac{\omega_k}{\omega_0}\right]^n \tag{A1}$$

for $n=1,2,3,\ldots$, and

$$g_n=\sum_k \frac{\sigma_k^2}{\omega_k^2}\left[\frac{\omega_k}{\omega_0}\right]^{n+1}\left[\frac{1}{e^{\hbar\beta\omega_k}-1}\right] \tag{A2}$$

for $n=1,2,3,\ldots$. Using Eq. (11) in the large-N limit, the first set of parameters can be expressed as

$$f_n=\frac{8\bar{\chi}^2\omega_a^{n-2}}{\hbar^2\pi\omega_0^n}\int_0^1 dy\, y^2(1-y^2)^{n/2} \tag{A3}$$

which yields

$$f_1=\frac{2\bar{\chi}^2}{\hbar^2\omega_0\omega_a} \tag{A4}$$

for $n=1$,

$$f_n=\frac{2\bar{\chi}^2\omega_a^{n-2}}{\hbar^2\pi\omega_0^n}\frac{\left[\frac{n-2}{2}\right]!}{\prod_{k=0}^{n/2}\left[\frac{n+1}{2}-k\right]} \tag{A5}$$

for n even, and

$$f_n=\frac{2\bar{\chi}^2\omega_a^{n-2}}{\hbar^2\pi\omega_0^n}\frac{\prod_{k=0}^{(n-3)/2}\left[\frac{n-2}{2}-k\right]}{\left[\frac{n+1}{2}\right]!} \tag{A6}$$

for n odd. Using Eq. (11) in the large-N limit, the parameters g_n are given by

$$g_n=\frac{8\bar{\chi}^2\omega_a^{n-1}}{\hbar^2\pi\omega_0^{n+1}}\int_0^1 dy\, y^n(1-y^2)^{1/2}\left[\frac{1}{e^{\hbar\beta\omega_a y}-1}\right]. \tag{A7}$$

Since we have not found a closed form expression for the integral, we compute Eq. (A7) using Simpson's rule. Our process is to have the computer program cycle through successively smaller grid sizes until the newest value of integral differs from the previous one by a predetermined small criterion. We have adjusted the criterion as required to assure that the final results are not adversely affected by the choice.

To obtain time derivatives through second and fourth orders we first expand $\dot{\chi}(t)$ in Eq. (77) to the fourth order in σ_k. Care must also be taken to expand the partition function Q defined in Eq. (81). Once the desired expansion is obtained, we take the time derivatives and evaluate them at $t=0$. To write the resulting expressions in terms of the parameters f_n and g_n, it also necessary that one expand some of the terms using the binomial expansion. We forego an exposition of this straightforward, but tedious algebra and present the final formula. For the time derivatives fourth order in σ_k we have

$$\begin{aligned}\frac{\sigma_0^{(n)}}{\omega_0^{2n}}=&1-\frac{16\eta n A_1}{\omega_0}+4A_1\sum_{j=1}^{2n}\binom{2n}{2j-1}f_{2j-1}+\frac{64\eta^2}{\omega_0^2}A_2 n(2n-1)\\
&-\frac{64\eta n}{\omega_0}A_3\sum_{j=1}^{n}\binom{2n-1}{2j-1}f_{2j-1}+8\sum_{j=1}^{n}\binom{2n}{2j-1}f_{2n-2j+1}\sum_{m=1}^{j}\binom{2j-1}{2m-1}f_{2m-1}\\
&+4\sum_{j=1}^{n}\binom{2n}{2j}(2g_{2j-1}+f_{2j})-\frac{64\eta n A_4}{\omega_0}\sum_{j=1}^{n-1}\binom{2n-1}{2j}(2g_{2j-1}+f_{2j})\\
&+16A_4\sum_{j=1}^{n}\binom{2n}{2j-1}f_{2n-2j+1}\sum_{m=1}^{j-1}\binom{2j-1}{2m}(2g_{2m-1}+f_{2m})\\
&+8\sum_{j=0}^{n-1}\binom{2n}{2j}(2g_{2n-2j-1}+f_{2n-2j})\sum_{m=1}^{j}\binom{2j}{2m}(2g_{2m-1}+f_{2m}),\end{aligned} \tag{A8}$$

where

$$A_1=2[\langle n\rangle_0+\beta\eta(\langle 4n^3+4n^2+n\rangle_0 - \langle n\rangle_0\langle 4n^2+4n+1\rangle_0)]+1\ , \quad \text{(A9)}$$

$$A_2=\langle 3n^2+3n+1\rangle_0\ , \quad \text{(A10)}$$

$$A_3=\langle 2n^2+2n+1\rangle_0\ , \quad \text{(A11)}$$

$$A_4=\langle 2n+1\rangle_0\ , \quad \text{(A12)}$$

and

$$\langle n^m\rangle_0=\frac{\sum_{n=0}^{\infty} e^{-\hbar\beta\omega_0 n} n^m}{\sum_{n=0}^{\infty} e^{-\hbar\beta\omega_0 n}}\ . \quad \text{(A13)}$$

The second-order expression is easily obtained from Eq. (97) by dropping terms fourth order in σ_k.

The computation of the exact time derivatives from Eq. (77) is a rather formidable task. Because one has to apply the formula for the derivative of products many times over, the number of terms grows very rapidly. This can be ameliorated to some extent by noting that the argument of the exponential and the argument of the cosine terms in Eq. (77) are zero at $t=0$. One can also speed up the evaluation program by precomputing the degeneracy factor for a given product of derivatives and only computing the given product once. For example, the second time derivative of the product $u(t)v(t)$ produces the terms $\dot{u}(t)\dot{v}(t)+\dot{u}(t)\dot{v}(t)$ which obviously should be computed as one term with degeneracy factor 2. These degeneracies are compounded by similar degeneracies which arise from the fact that the time dependence in Eq. (77) is contained in an exponential factor and the arguments of trigonometric functions. We exploit formula 0.430.1 of Gradshteyn and Ryzhik[44] to compute these degeneracies. We have incorporated all these features in our program. With these enhancements we have only succeeded in computing up to the tenth moment (or twentieth time derivative) because of the large number of terms. Nevertheless, this is sufficient for us to make comparisons of the exact treatment with the second- and fourth-order approximations.

[1]A. S. Davydov and N. I. Kislukha, Phys. Status Solidi B **59**, 465 (1973).

[2]A. S. Davydov and N. I. Kislukha, Zh. Eksp. Teor. Fiz. **71**, 1090 (1970) [Sov. Phys. JETP **44**, 571 (1976)].

[3]A. S. Davydov, Phys. Scr. **20**, 387 (1979).

[4]H. Fröhlich, Adv. Phys. **3**, 325 (1954).

[5]S. Takeno, Prog. Theor. Phys. **69**, 1798 (1983); **71**, 395 (1984); **73**, 853 (1985).

[6]X. Wang, D. W. Brown, and K. Lindenberg, Phys. Rev. B **39**, 5366 (1989).

[7]D. W. Brown, B. J. West, and K. Lindenberg, Phys. Rev. A **33**, 4104 (1986).

[8]D. W. Brown, B. J. West, and K. Lindenberg, Phys. Rev. A **33**, 4110 (1986).

[9]B. Mechtly and P. B. Shaw, Phys. Rev. B **38**, 3075 (1988).

[10]M. Wagner and A. Kongeter, J. Chem, Phys. **91**, 3036 (1989).

[11]W. Rhodes and A. Nicholls, Phys. Rev. Lett. **64**, 1174 (1990).

[12]P. S. Lomdahl and W. C. Kerr, in *Proceedings of the NATO Workshop on Localization of Energy in Proteins,* edited by A. Scott and P. C. Christiansen (Hanstholm, Denmark, 1989).

[13]A. C. Scott, Philos. Trans. R. Soc. A **315**, 423 (1985).

[14]A. S. Davydov, Zh. Eksp. Teor. Fiz. **78**, 789 (1980) [Sov. Phys. JETP **51**, 397 (1980)].

[15]P. S. Lomdahl and W. Kerr, Phys. Rev. Lett. **55**, 1235 (1985).

[16]P. S. Lombdahl and W. C. Kerr, in *Physics of Many Particle Systems,* edited by A. S. Davydov (Nauka Dumka, Kiev, 1988).

[17]D. M. Alexander and J. A. Krumhansl, Phys. Rev. B **33**, 7172 (1986).

[18]G. Careri, U. Buontempo, F. Galluzzi, A. C. Scott, E. Gratton, and E. Shyamsunder, Phys. Rev. B **30**, 4689 (1984).

[19]L. Cruizeiro, J. Halding, P. L. Christiansen, O. Skovgaard, and A. C. Scott, Phys. Rev. A **37**, 880 (1988).

[20]J. P. Cottingham and J. W. Schweitzer, Phys. Rev. Lett. **62**, 1792 (1989).

[21]A. Migliori, P. M. Maxton, A. M. Clogston, E. Zirngiebl, and M. Lowe, Phys. Rev. B **38**, 13 464 (1988).

[22]G. W. Ford, M. Kac, and P. Mazur, J. Math. Phys. **6**, 504 (1965).

[23]D. W. Brown, K. Lindenberg, and B. J. West, J. Chem. Phys. **84**, 1574 (1986).

[24]D. W. Brown, K. Lindenberg, and B. J. West, J. Chem. Phys. **87**, 6700 (1987).

[25]D. C. Langreth, Phys. Rev. B **1**, 471 (1970).

[26]H. K. McDowell, J. Chem. Phys. **87**, 4859 (1987).

[27]S. A. Adelman, J. Chem. Phys. **71**, 4471 (1979).

[28]S. A. Adelman, Adv. Chem. Phys. **44**, 143 (1980).

[29]S. A. Adelman, J. Chem. Phys. **74**, 4646 (1981).

[30]S. A. Adelman, J. Chem. Phys. **73**, 3145 (1980).

[31]M. Berkowitz, C. L. Brooks, and S. A. Adelman, J. Chem. Phys. **72**, 3889 (1980).

[32]C. L. Brooks, M. Berkowitz, and S. A. Adelman, J. Chem. Phys. **73**, 4353 (1980).

[33]S. A. Adelman and M. W. Balk, J. Chem. Phys. **81**, 5117 (1981).

[34]S. A. Adelman, Adv. Chem. Phys. **53**, 61 (1983).

[35]S. A. Adelman, J. Chem. Phys. **75**, 5837 (1981).

[36]H. K. McDowell, J. Chem. Phys. **85**, 6034 (1986).

[37]H. K. McDowell, J. Chem. Phys. **86**, 1497 (1987).

[38]H. K. McDowell, J. Chem. Phys. **86**, 5763 (1987).

[39]H. K. McDowell, Nucl. Phys. **B5A**, 247 (1988).

[40]H. K. McDowell, Chem. Phys. **132**, 59 (1989).

[41]H. K. McDowell, J. Chem. Phys. **93**, 6723 (1990).

[42]W. H. Press, B. P. Flannery, S. A. Teukolsky, and W. T. Vetterling, *Numerical Recipes* (Cambridge University Press, Cambridge, England, 1986), p. 523.

[43]H. K. McDowell and A. M. Clogston, J. Stat. Phys. (to be published).

[44]I. S. Gradshteyn and I. M. Ryzhik, *Tables of Integrals, Series and Products* (Academic, New York, 1980), p. 19.